Biochemical Journal (2021) **478** 1525–1545
https://doi.org/10.1042/BCJ20201002

PORTLAND PRESS

Research Article

Synergy and allostery in ligand binding by HIV-1 Nef

Abdullah Aldehaiman[1], Afaque A. Momin[1], Audrey Restouin[2], Luyao Wang[1], Xiaoli Shi[3], Safia Aljedani[1], Sandrine Opi[2], Adrien Lugari[4], Umar F. Shahul Hameed[1], Luc Ponchon[5], Xavier Morelli[2], Mingdong Huang[6], Christian Dumas[7], Yves Collette[2] and Stefan T. Arold[1,7]

[1]King Abdullah University of Science and Technology (KAUST), Computational Bioscience Research Center (CBRC), Biological and Environmental Science and Engineering (BESE), Thuwal 23955-6900, Saudi Arabia; [2]CRCM, CNRS, INSERM, Institut Paoli-Calmettes, University Aix-Marseill1715e, 13009 Marseille, France; [3]State Key Laboratory of Structural Chemistry, Fujian Institute of Research on the Structure of Matter, Chinese Academy of Sciences, 155 Yang Qiao Xi Lu, Fuzhou, Fujian 350002, China; [4]Sartorius Stedim FMT S. A.S, ZI Les Paluds - Avenue de Jouques, 13781 Aubagne Cedex, France; [5]Laboratoire CiTCoM, CNRS UMR 8038, Université de Paris, 4 Avenue de l'observatoire, 75270 Paris, France; [6]National Local Joint Research Center on Biomedical Photodynamic Technology, Fuzhou University, 2 Wulong River North Blvd, Sunshine Building Rm 613S, Minhou District, Fuzhou, Fujian 350108, China; [7]Centre de Biochimie Structurale, CNRS, INSERM, Université de Montpellier, 34090 Montpellier, France

Correspondence: Stefan T. Arold (stefan.arold@kaust.edu.sa)

OPEN ACCESS

The Nef protein of human and simian immunodeficiency viruses boosts viral pathogenicity through its interactions with host cell proteins. By combining the polyvalency of its large unstructured regions with the binding selectivity and strength of its folded core domain, Nef can associate with many different host cell proteins, thereby disrupting their functions. For example, the combination of a linear proline-rich motif and hydrophobic core domain surface allows Nef to bind tightly and specifically to SH3 domains of Src family kinases. We investigated whether the interplay between Nef's flexible regions and its core domain could allosterically influence ligand selection. We found that the flexible regions can associate with the core domain in different ways, producing distinct conformational states that alter the way in which Nef selects for SH3 domains and exposes some of its binding motifs. The ensuing crosstalk between ligands might promote functionally coherent Nef-bound protein ensembles by synergizing certain subsets of ligands while excluding others. We also combined proteomic and bioinformatics analyses to identify human proteins that select SH3 domains in the same way as Nef. We found that only 3% of clones from a whole-human fetal library displayed Nef-like SH3 selectivity. However, in most cases, this selectivity appears to be achieved by a canonical linear interaction rather than by a Nef-like 'tertiary' interaction. Our analysis supports the contention that Nef's mode of hijacking SH3 domains is a virus-specific adaptation with no or very few cellular counterparts. Thus, the Nef tertiary binding surface is a promising virus-specific drug target.

Introduction

Nef is an accessory protein that enhances the virulence and pathogenesis of human and simian immunodeficiency viruses (HIV and SIV, respectively) [1,2]. HIV viruses that lack functional Nef protein fail to cause acquired immunodeficiency syndrome in infected persons [3–6]. Nef has therefore been suggested to be a promising drug target.

Nef contributes to disease progression via its capacity to disrupt several functions of the host cell. Nef alters the protein composition of the host cell surface by down-regulating the transmembrane proteins involved in immune signalling and viral entry, including CD3, CD4, CD8, CD28, CXCR4, CCR5, SERINC3, SERINC5, and antigen-loaded MHC-II [reviewed in [7]]. Additionally, Nef up-regulates the surface expression of other factors, including TNF, DC-SIGN, and LIGHT [8,9]. Other functions of Nef include promoting T-cell activation [10,11] and lymphocyte chemotaxis [12].

Received: 24 December 2020
Revised: 29 March 2021
Accepted: 31 March 2021

Accepted Manuscript online: 31 March 2021
Version of Record published: 21 April 2021

Biochemical Journal (2021) **478** 1525–1545
https://doi.org/10.1042/BCJ20201002

Nef also disrupts intracellular signalling primarily through its interactions with cytoplasmic kinases, including members of the Src and Tec/Bt kinase families, PAK2, and PI3 kinase [13–18]. Collectively, these actions promote the immune evasion of infected cells and enhance viral release, spread, and infectivity.

Nef is a noncatalytic protein that causes these effects by interacting with a multitude of cellular proteins. The molecular bases for some of these interactions have been identified. Initial NMR and crystallographic studies have shown that Nef comprises a myristoylated flexible N-terminal arm (residues 1–70; we use the numbering of the LAI isolate unless stated otherwise), and a folded core domain (residues 71–206) that harbours a long flexible loop (residues 148–179) (Figure 1A) [19–23]. Both the core domain and flexible regions contain important ligand-binding sites [1,7].

Subsequent structural studies have revealed the molecular determinants of Nef's capacity to disrupt Src kinases by interacting closely with their SH3 domains [20,22,24]. In addition to its canonical 'linear' proline-rich motif P_{72}xxPxR (where x is any amino acid), Nef uses an extended surface provided by its folded core to bind to Src family SH3 domains. This resulting 'tertiary' binding mode increases the interaction surface along with affinity and selectivity for SH3 domains, compared with the canonical linear interaction between proline-rich motifs and SH3 domains [1,20,22]. One SH3 residue, located in the arginine (R) position of the arginine–threonine (RT) loop (residue number 96 in Fyn, a kinase from the Src family), was shown to primarily affect the binding affinity by interacting with a pocket on the core surface of Nef [25]. This pocket is hydrophobic in HIV-1 Nef, and more hydrophilic in SIV Nef. Consequently, HIV-1 Nef binds stronger to those kinases whose SH3 domain has a hydrophobic residue at the R position, whereas SIV Nef prefers charged or polar residues [20,26].

Additionally, the rigidity of the SH3 RT loop also influences the affinity to Nef [27]. The RT loop needs to bend to bind to Nef. Therefore, SH3 domains where the RT loop is stabilized by an extensive hydrogen-bond

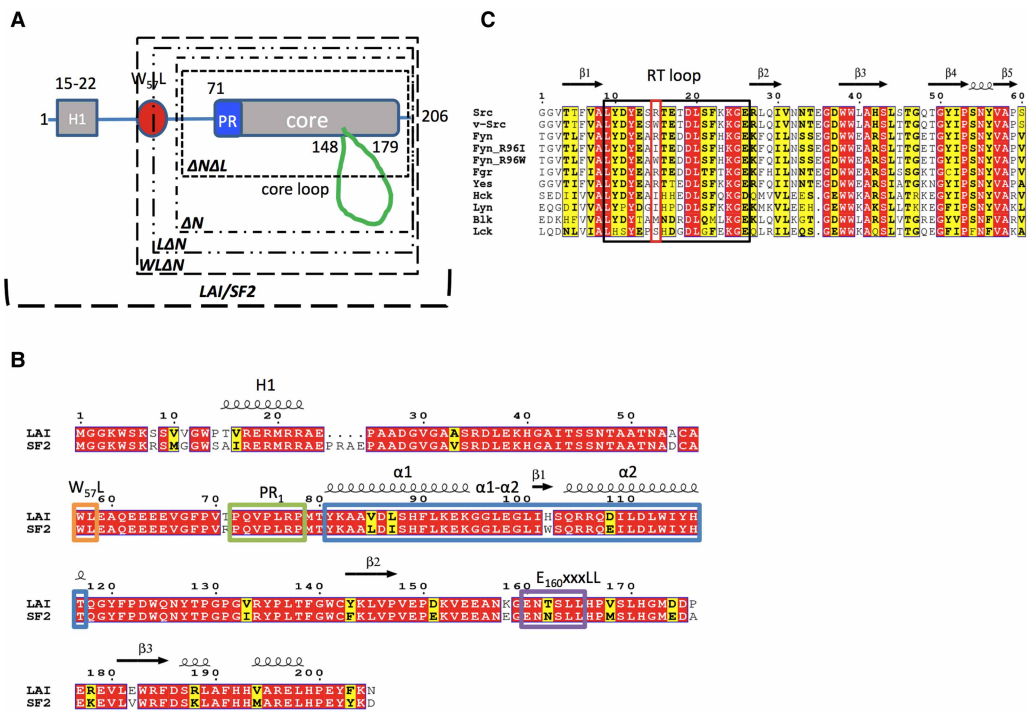

Figure 1. Overview of the constructs used.

(**A**) Schematic drawing of the Nef constructs in which key residues, such as W_{57}L and the proline-rich region (PR, including the P_{72}xxPxR motif), are shown. (**B**) Sequence alignment between LAI and SF2 Nef in which the key motifs discussed in the paper are highlighted: H1, brown; W_{57}L, orange; PR, green; α1–α2, blue; and the E_{160}xxxLL endocytosis motif, purple. (**C**) Sequence alignment of all of the SH3 domains investigated. The RT loop is boxed in black and the R position within it is highlighted in red. In both sequence alignments, residues with similar physicochemical properties are presented in bold black letters on a yellow background. Conserved residues are highlighted in red.

network (such as that seen in Fyn) need to pay a higher enthalpic cost for binding to Nef than SH3 domains with a more flexible RT loop (as present in Hck, another member of the Src family).

SH3 binding by Nef activates Hck by outcompeting those intramolecular interactions that maintain Hck in its catalytically inactive 'closed' conformation [28,29]. SH3-dependent activation by Nef has also been observed for Lyn and c-Src in a *Saccharomyces cerevisiae* assay [30], but not in an *in vivo* transformation assay [31]. The yeast assay also failed to show activation of Fgr, Fyn, Lck, or Yes by Nef. Hence, although Nef-targeted kinases have been shown to play roles in HIV replication, infectivity, MHC-1 down-regulation, and pro-inflammatory vesicle release [16,17,32,33], the molecular mechanism underlying these effects remains to be fully elucidated.

Structural studies have also revealed the mechanism through which Nef molecules hijack the host cell's trafficking machinery by serving as an adaptor between AP1 and MHC-I or between AP2 and CD4 [7,34–37]. Similar to its interactions with Src family SH3 domains, Nef uses its core domain along with the linear recognition motifs that are located on its flexible regions to firmly bind to AP1 or AP2. However, Nef binds AP1 differently than AP2. Nef binds to the μ1 subunit of AP1, and a part of the MHC-I cytoplasmic tail is sequestered in a groove formed between AP1 and Nef. In the case of AP2, Nef binds to the α2, β2, and σ2 subunits of AP2. In contrast, Nef binds to the α2, β2, and σ2 subunits of AP2. In this association, Nef uses its E_{160}xxxLL motif, located in the core domain loop, to mimic acidic dileucine motifs of cellular AP2 cargos. In parallel, Nef uses a core domain binding pocket to engage a part of the cytoplasmic CD4 tail [34,37], thus connecting CD4 to AP2. Despite these differences, the binding sites of CD4 and MHC-I on Nef show partial overlap [37].

Collectively, these studies show that Nef's strong polyvalent interactions result from a combination of the following two factors: (1) the multivalency that is intrinsic to flexible protein–protein interaction motifs, and (2) the high specificity and affinity resulting from the large binding surface offered by a 3D folded domain. Nef's composition of 50% tertiary structure and 50% flexible regions constitutes an optimal structural framework for this strategy. However, the resulting capacity of Nef to bind to a high number of cellular targets, raises the question of whether binding to one target affects Nef's associations with other targets. More specifically, has Nef evolved allosteric mechanisms for creating synergies between sets of ligands that contribute to the same cellular function while excluding others? In this study, we combined structural and functional studies to identify crossreactivity in selected intra- and intermolecular associations.

Materials and methods

Production of recombinant proteins

Fyn SH3 (Fyn_{R96}, Fyn_{R96I}, and Fyn_{R96W}) and Nef (SF2, LAI, ΔN, ΔNΔL, and WLΔN) constructs were expressed in *Escherichia coli* Bl21 (DE3) cells using a pGEX-2T expression vector containing an N-terminal GST tag with a thrombin cleavage site (Fyn_{R96W}; Nef WLΔN), a pET42a expression vector containing a C-terminal hexa-His tag (Fyn_{R96} and Fyn_{R96I}), or a pET23d expression vector containing a C-terminal hexa-HIS tag (SF2). Nef ΔN, Nef ΔNΔL, and LAI were expressed using a pJEx411c expression vector (pJExpress411, originally from DNA 2.0, CA [38]) containing an N-terminal GST tag with 3C protease cleavage site. The bacterial cells were cultured at 37°C in 2xYT broth containing 100 μg/ml ampicillin (all Fyn, Nef WLΔN, and SF2) or 50 μg/ml kanamycin (Nef ΔN, Nef ΔNΔL, and LAI). When the optical density at 600 nm reached 0.6–0.8, protein expression was induced using 0.2 mM IPTG (Fyn constructs) or 0.5 mM IPTG (Nef constructs) and proceeded overnight at 18°C. The cells were then harvested and resuspended in 50 mM Tris (pH, 8.0), 200 mM NaCl, 2 mM EDTA (excluded in His tag purification), 1 mM DTT, one tablet of EDTA-free protease inhibitor (Roche) per 50 ml of resuspension, 1% triton, and 0.4 mg/ml lysozyme. Cells were lysed via sonication and pelleted by centrifugation at 87 207×***g*** for 45 min at 4°C.

All proteins were purified using HIS-affinity columns (Fyn_{R96}, Fyn_{R96I}, and SF2), or GST-affinity columns (Fyn_{R96W} and LAI, WLΔN, ΔN, ΔNΔL) followed by mono Q 10/100 GL (GE Healthcare) anion exchange chromatography and HiLoad Superdex75 16/60 (GE Healthcare) size-exclusion chromatography . Protein purity was analyzed using SDS–PAGE gels. The buffer used were 50 mM Tris (pH, 8.0), 200 mM NaCl, 2 mM EDTA (excluded for HIS column), and 1 mM DTT. Proteins were dialyzed in the same buffer but with 100 mM NaCl for the Mono Q column.

Crystallization and structure determination

For the initial crystallization experiments for the apo Fyn_{R96I} or Fyn_{R96W} SH3 domains, the domains were dialyzed against 20 mM Tris (pH 8.0), 150 mM NaCl, and 1 mM EGTA and concentrated by ultrafiltration to 5–

Biochemical Journal (2021) 478 1525–1545
https://doi.org/10.1042/BCJ20201002

8 mg/ml. Crystallization was performed by vapour diffusion (Fyn_{R96I}, sitting-drop at 18°C; Fyn_{R96W}, hanging-drop at 4°C) where 1 μl of protein solution was mixed with 1 μl of well solution (0.2 M ammonium acetate, 0.1 M sodium citrate [pH, 5.6], and 1.0 M lithium sulfate for Fyn_{R96I} [crystal form I]; 0.2 M ammonium acetate, 0.1 M Tris–HCl [pH, 5.6], and 30% v/v MPD for Fyn_{R96I} [crystal form II]; and 2 M ammonium sulfate, 2% PEG 400, and 0.1 M Tris [pH, 9.1] for Fyn_{R96W} SH3). PEG 200 (25%) was used as a cryoprotectant for Fyn_{R96I} (crystal form I). Data were recorded at 100 K (Fyn_{R96I}) or 295 K (Fyn_{R96W}) at $\lambda = 1.54$ Å, using the Rigaku 200 X-ray generator, confocal multilayer mirrors (Osmic), and a MAR300 image plate detector. Data were integrated, merged, and scaled using Mosflm [39] and Scala [40] (Supplementary Table S1). All data were checked using ContaMiner [41], and the initial phases were determined by molecular replacement using Molrep [42]. For Fyn_{R96I} (crystal form I) and Fyn_{R96W} SH3, Fyn_{R96} SH3 was used as a template (Protein Data Bank PDB ID 1SHF) [43]. Fyn_{R96I} (form I) was used as a template for Fyn_{R96I} (crystal form II). The structures were refined using Refmac [44] and COOT [45] (Supplementary Table S1; PDB IDs, 3HOF, 3HOH, and 3HOI).

In a second round of crystallization experiments, Fyn_{R96I} with a C-terminal hexahistidine tag (see [46] for cloning details) was crystallized in 0.1 M citric acid at a pH of 3.5 and 25% w/v polyethylene glycol 3,350. The crystals were cryoprotected with 25% glycerol and diffracted to 1.34 Å resolution at the SOLEIL synchrotron beamline PROXIMA 2A, France. The hexahistidine tag stabilized the crystal packing (Supplementary Figure S1A, Supplementary Table S1; PDB ID 6IPY). Fyn_{R96W} SH3 was crystallized in 0.08 M sodium acetate trihydrate at a pH of 4.6, 1.6 M ammonium sulfate, 20% v/v glycerol, and 50 mM 18-crown-6. Crystals diffracted to a 1.57 Å resolution at PROXIMA 2A. The CCP4 online version of MoRDa was used to determine the structures [47], followed by rebuilding through BUCCANEER [48], and manual and automated refinement (REFMAC5, PHENIX) [49,50]. Two 18-crown-6 molecules were identified (Supplementary Figure S1B, Supplementary Table S1; PDB ID 6IPZ).

Crystals of the HIV-1 Nef_{58-205}–Fyn_{R96W} SH3 complex were obtained via the hanging-drop vapour diffusion method at 18°C–20°C. Before crystallization, stoichiometric amounts of Nef_{58-205} and Fyn_{R96W} SH3 were mixed, concentrated to obtain 0.35 mM of Nef–SH3 complex, and filtered. Then, 1 μl samples of this solution were mixed with 1 μl of the reservoir buffer containing 0.25–0.3 M sodium potassium tartrate, 0.5 M bicine buffer (pH, 8.4), and one critical micelle concentration β-D-octylglucopyranoside. Crystals were cryoprotected by rapid transfer into 28% glycerol, 0.3 M sodium potassium tartrate, and 0.5 M bicine buffer (pH, 8.4). The crystals were then flash-cooled in liquid nitrogen, and data were collected at 100 K at the FIP beamline at the European Synchrotron Radiation Facility (Grenoble, France) using the MAR345 image plate detector. The images were processed and scaled using Mosflm [39] and Scala [40]. Crystal phases were obtained by molecular replacement using LΔN–Fyn_{R96} and WLΔN–Fyn_{R96I} SH3 complex structures as templates (PDB IDs 1AVZ and 1EFN). The structure was refined using Refmac [49] and Phenix [50] (Supplementary Table S2; PDB ID 4D8D).

SF2 Nef–Fyn_{R96I} SH3 complex crystals were obtained by the sitting-drop vapour diffusion method at 18°C–20°C. Before crystallization, stoichiometric amounts of full-length SF2 Nef and Fyn_{R96I} SH3 were mixed, concentrated to obtain 1 mM of Nef–SH3 complex, and filtered. Then, 1 μl of this solution was mixed with 1 μl of the reservoir buffer containing 0.10 M calcium acetate hydrate, 0.10 M sodium acetate buffer (pH, 4.5), and 10% w/v PEG 4000. The crystals were cryoprotected by a rapid transfer into 28% glycerol, 0.10 M calcium acetate hydrate, 0.10 M sodium acetate buffer (pH, 4.5), and 10% w/v PEG 4000. All data for SF2 Nef–Fyn_{R96I} SH3 were collected at 100 K at PROXIMA 2A with an EIGER 9 M detector (proposal numbers 2016 0098, 20161236, and 20170193). Data from three crystals were processed, scaled, and combined using XDS as implemented in the XDSme pipeline (unmerged data are available at https://doi.org/10.25781/KAUST-8CV15). STARANISO [51] was used for merging the three datasets and for establishing the anisotropic resolution limits. Initial phases were determined using MoRDa [47] with the PDB ID 4D8D as the molecular replacement template (Q score, 0.834). The structure was manually corrected using COOT and refined using LORESTR [52] (Ramachandran outliers/favourite 2.53/91.14%) (Supplementary Table S2; PDB ID 7D7S).

Molecular dynamics simulations

Molecular dynamics simulations were carried out in triplicates for apo-Nef (Nef-A) and Nef in a complex with Fyn_{R96I} (Nef-C), using the 2.5 Å resolution crystal structure of LAI Nef_{T71R} bound to Fyn_{R96I} (PDB ID 1EFN) as a template. MD simulations were performed using GROMACS 2018 [53] with the AMBER14SB force field [54]. Each protein was inserted into a cubic box filled with TIP3P water molecules. Box size was chosen to have a minimum distance of 10.0 Å from the protein edges to the box sides. The system was neutralized with

Na^+ and Cl^- ions. Energy minimization was performed followed by equilibration using isothermal ensemble dynamics (NVT) with a velocity-rescale thermostat [55] for computing velocities and atom positions. The structures were further equilibrated for 2 ns with isothermal–isobaric ensemble dynamics (NPT). Periodic boundary conditions were applied in the X, Y, and Z directions. Final production simulations were conducted using NPT for 200 ns in triplicate. The temperature was kept constant at 300 K using a velocity-rescale thermostat [55] ($\tau T = 0.1$ ps) and 1 bar pressure was maintained using a Parrinello–Rahman barostat [56] ($\tau P = 2.0$ ps). Electrostatic interactions beyond 12 Å were evaluated using the particle mesh Ewald method [57]. The LINear Constraint Solver algorithm (LINCS) [58] was used to constrain the bond lengths and the Output trajectories were analyzed using GROMACS 2018 and PyMol (www.pymol.org).

Microscale thermophoresis

Proteins were labelled using the Monolith protein labelling kit RED-NHS 2nd Generation. The concentrations of the labelled protein ranged from 10 to 50 nM. The concentrations of unlabelled preincubated SH3 and H1 were 50 μM and 1 mM, respectively. Measurements were performed at 25%–50% LED and 40% microscale thermophoresis powers. Data were analyzed using the program provided by Nanotemper Technologies. All MST experiments were performed in 50 mM Tris (pH, 8.0), 200 mM NaCl, 2 mM EDTA (excluded in HIS tag purification), and 1–2 mM DTT at 20°C.

Isothermal titration calorimetry

Isothermal titration calorimetry (ITC) experiments were performed on MicroCal PEAQ-ITC (Malvern Panalytical) using the 19-injection standard method at 25°C. All proteins were dialyzed and degassed in 20 mM sodium phosphate (pH, 7.5), 150 mM NaCl, 2 mM EDTA, and 1–2 mM TCEP. The protein concentrations in the cell ranged from 20 to 75 μM and were 10-fold higher in the syringe. The measurements and data were analyzed using the software provided by Origin.

Yeast two-hybrid (Y2H) screens

Yeast two-hybrid (Y2H) screenings were performed as previously reported [59].

Bioinformatics analysis

Bioinformatics analysis for Y2H was performed using RaptorX for property and structure predictions and the ELM database for the identification of SH3 binding motifs [60,61].

Results and discussion

Flexible Nef regions have specific thermodynamic effects on SH3 binding

To assess the influence of the flexible regions of Nef on ligand binding, we recombinantly produced the following HIV-1 LAI Nef constructs: (i) full-length Nef, (ii) Nef with a deletion of the N-terminal arm while retaining the $W_{57}L$ motif that is implicated in CD4 binding (residues 56–205; WLΔN); (iii) Nef with a deletion of the N-terminal arm that lost W_{57} and retained L_{58} (residues 58–205; LΔN), corresponding to the product of Nef cleavage by the HIV-1 protease [62]; (iv) Nef with a deletion of the N-terminal arm that lost the $W_{57}L$ motif (residues 60–205; ΔN); and (v) a Nef ΔN construct with an additional truncation of the core loop to eliminate the E_{160}xxxLL endocytosis motif (residues 60–158;174–205; ΔNΔL) (Figure 1A). We also included the full-length SF2 Nef to test the isolate specificity of the effects. Compared with the LAI isolate, SF2 Nef has a four amino-acid insertion at the N-terminal region and a $T_{71}R$ substitution that enhances binding to Src family SH3 domains [28,63] (Figure 1B).

To test the effect of the SH3 R position on Nef binding, we produced SH3 domain constructs that were engineered to have different side chains at this position. We used Fyn_{R96}, the Fyn SH3 wild-type where the R position is a long and positively charged arginine; Fyn_{R96I}, where the R position is filled by a medium-sized hydrophobic isoleucine as in Hck; and Fyn_{R96W} where the R position is occupied by a large and hydrophobic tryptophan, as in the *Rous sarcoma* virus v-Src (Figure 1C).

We measured the thermodynamic parameters of the interactions between the three SH3 variants and different Nef constructs using ITC (Table 1). In agreement with previous studies [25,27], the hydrophobic substitutes Fyn_{R96I} and Fyn_{R96W} showed markedly higher affinities than Fyn_{R96} by better matching the hydrophobic Nef pocket. Compared with LAI Nef, SF2 Nef showed a higher affinity for all SH3 variants. This observation can be

Biochemical Journal (2021) **478** 1525–1545
https://doi.org/10.1042/BCJ20201002

Table 1 Influence of the flexible regions on the thermodynamics of SH3 binding by Nef

Nef–Fyn	*N*	K_d (μM)	ΔG (kJ/mol)	ΔH (kJ/mol)	TΔS (kJ/mol)
ΔNΔL–Fyn_{R96}[2]	1[1]	24.3 ± 15.0	−26.3 ± 1.50	−14.0 ± 10.0	12.3 ± 10.0
ΔNΔL–Fyn_{R96I}	0.97 ± 0.10	3.86 ± 0.60	−31.0 ± 0.40	−34.0 ± 5.67	−3.02 ± 5.56
ΔNΔL–Fyn_{R96W}	0.98 ± 0.04	0.78 ± 0.22	−34.9 ± 0.76	−46.7 ± 3.70	−11.8 ± 2.94
ΔN–Fyn_{R96}[2]	1[1]	83.3 ± 15.0	−23.3 ± 1.50	−34.3 ± 10.0	−11.0 ± 10.0
ΔN–Fyn_{R96I}	0.87 ± 0.03	5.06 ± 0.96	−30.3 ± 0.47	−39.7 ± 0.34	−9.40 ± 0.73
ΔN–Fyn_{R96W}	0.90 ± 0.02	1.28 + 0.45	−33.7 ± 0.88	−56.5 ± 8.68	−22.7 ± 9.56
WLΔN–Fyn_{R96}[2]	1[1]	50.8 ± 15.0	−24.5 ± 1.50	−14.2 ± 10.0	10.3 ± 10.0
WLΔN–Fyn_{R96I}	1.01 ± 0.05	7.55 ± 1.57	−29.3 ± 0.54	−21.5 ± 2.18	7.77 ± 2.71
WLΔN–Fyn_{R96W}	0.94 ± 0.04	1.45 ± 0.40	−33.4 ± 0.76	−29.3 ± 0.37	4.16 ± 0.52
LAI–Fyn_{R96}[2]	1[1]	58.5 ± 8.44	−24.2 ± 0.68	−45.9 ± 10.5	−21.7 ± 10.8
LAI–Fyn_{R96I}	0.93 ± 0.01	0.79 ± 0.08	−34.9 ± 0.23	−40.7 ± 1.07	−5.80 ± 1.30
LAI–Fyn_{R96W}	0.96 ± 0.02	1.43 ± 0.10	−33.4 ± 0.15	−50.0 ± 1.29	−16.6 ± 1.41
SF2–Fyn_{R96}[2]	1[1]	28.7 ± 8.72	−26.1 ± 0.76	−59.2 ± 10.3	−33.2 ± 11.01
SF2–Fyn_{R96I}	0.98 ± 0.04	0.02 ± 0.00	−43.5 ± 0.07	−77.2 ± 5.68	−33.7 ± 5.75
SF2–Fyn_{R96W}	0.91 ± 0.03	0.12 ± 0.03	−39.5 ± 0.58	−56.6 ± 6.00	−17.1 ± 5.58

Isothermal titration calorimetry (ITC) data were obtained at 25°C by titrating Fyn SH3 domains from the syringe onto Nef in the measurement cell. Values are given as mean ± SD ($n = 3$) except for the following two cases:
[1]The C-value of the titration was too low to establish the stoichiometry *N*, and *N* has been fixed to 1 based on the known Nef–SH3 stoichiometry
[2]Due to low heat and C-values, instrument errors appeared to underestimate the real uncertainty of the data analysis. For these cases, the errors shown were estimated based on observed variations in data analysis. The ITC data are shown in Supplementary Figure S2.

explained, at least in part, by the additional hydrogen bond formed by R_{71} in SF2 Nef [63]. However, our titrations also provided the following additional insights:

(i) In all of the LAI Nef titrations, the binding thermodynamics of Fyn_{R96I} were overall similar to those of Fyn_{R96W}; however, Fyn_{R96W} consistently had more favourable enthalpy (ΔH) and less favourable entropy (ΔS). The less favourable ΔS of the most hydrophobic R mutant, Fyn_{R96W}, was unexpected because hydrophobic interactions normally contribute favourably to ΔS [64]. This observation suggested that unknown additional factors influenced the thermodynamics of binding.

(ii) Truncated Nef constructs bound approximately four times more strongly to Fyn_{R96W} than to Fyn_{R96I}, whereas full-length LAI and SF2 Nef bound stronger to Fyn_{R96I} than to Fyn_{R96W}. The affinity to the Fyn_{R96} SH3 domain was weak for all Nef constructs ($K_d > 25$ μM) and did not vary significantly. Thus, the presence of the N-terminal residues 1–55 increased the affinity of Nef specifically for the SH3 isoleucine variant.

(iii) Compared with Fyn_{R96I}, Fyn_{R96} bound ∼10 times more weakly to the truncated LAI constructs. When full-length Nefs were used, the difference in affinity between Fyn_{R96} and the other SH3 variants increased to 50-fold (LAI) and 200-fold (SF2). Although precise thermodynamic parameters could not be established for Fyn_{R96} due to the low C-values of the Fyn_{R96} binding curves, this observation suggested that the presence of the N-terminal segment increased the selectivity between Fyn_{R96} and the other two variants.

(iv) WLΔN showed significantly different thermodynamics from the other LAI titrations. WLΔN showed favourable ΔH and ΔS, whereas in all other LAI titrations, an approximately two-fold more favourable ΔH compensated for an unfavourable ΔS. This WLΔN-specific irregularity suggested that the $W_{57}L$ dipeptide promotes a thermodynamic contribution to SH3 binding that disappears once the full N-terminal segment is present.

Together, our ITC analysis showed that the presence of the flexible Nef regions affected the affinity and specificity of the association with SH3, and that these effects were specific to the motifs present in the flexible Nef regions.

Biochemical Journal (2021) 478 1525–1545
https://doi.org/10.1042/BCJ20201002

Presence of SH3 domains influences binding of the N-terminal Nef helix

Our ITC data suggested that the presence of the flexible N-terminal Nef residues influenced the association of Nef with SH3 domains. This Nef region contains an amphipathic helix (termed H1, comprising residues 15–22 in LAI; Figure 1A) that helps to anchor Nef to the charged lipid headgroups of the cellular membrane [23]. In structural studies of full-length Nef, this H1 helix has been observed to bind to the hydrophobic groove formed by the core helices α1 and α2 and the connecting residues (see PDB IDs 6CRI, 4EN2, and 6CM9). In this report, we refer to this region as the α1–α2 groove. This groove is adjacent to, but not overlapping with, the SH3-binding site [35,36].

We synthesized a Nef fragment containing H1 (residues 8–26) to test its affinity for the different Nef constructs in the presence or absence of the SH3 Fyn_{R96I} and Fyn_{R96W} variants. We used microscale thermophoresis (MST) for this experiment because it can measure low affinities as well as assess the effect of the presence of one ligand (preincubated at constant concentration with the labelled protein) on the binding of a second ligand (titrated as a dilution series). We preincubated fluorescently labelled Nef with SH3 domains before titrating H1. To ensure that most Nef bound to the SH3 domain, we used a constant concentration of 50 μM ($\sim 10 \times K_d$) of SH3 domains. We did not include the Fyn_{R96} SH3 here because its low affinity meant that we were unable to reach a concentration of $10 \times K_d$.

In MST experiments without SH3 domains, H1 bound to the core domain-only Nef ΔNΔL with a low affinity ($K_d \sim 300$ μM). The presence of additional flexible regions further decreased this affinity. The core loop containing Nef ΔN bound to H1 with a K_d of 700 μM, Nef WLΔN bound H1 with $K_d > 1$ mM, and full-length LAI and SF2 showed no binding at all. The presence of either Fyn_{R96I} or Fyn_{R96W} SH3 domains increased the affinity of H1 for Nef ΔNΔL and ΔN by approximately two-fold (Figure 2A–F, Table 2). WLΔN also showed a two-fold increase in the affinity for H1 when preincubated with Fyn_{R96I}. However, the effect of Fyn_{R96W} could not be determined from the MST data due to the low amplitude of the signal change. However, preincubation with SH3 domains did not result in a significant binding signal of H1 to the full-length Nefs.

Finally, we investigated whether the effect observed was mutual, i.e. whether preincubation of Nef with H1 also increased the affinity of Nef for SH3 domains. We chose ΔNΔL for this experiment, as it had the highest affinity for H1. We observed that the presence of H1 significantly increased the affinity of ΔNΔL for Fyn_{R96I} (Figure 2G, Table 2).

These data demonstrated that the presence of SH3 domains can enhance the association of H1 with the hydrophobic α1–α2 groove and *vice versa*. However, the more flexible regions were included, the lower was the affinity of Nef for H1. Full-length Nefs did not show any binding, possibly because their own H1 motifs outcompeted the H1 peptide. The $W_{57}L$ motif was found to back-bind to the α1–α2 groove in the apo-Nef NMR structure (2NEF) [19], which explains its competition with H1. However, the competition between H1 and the core loop was unexpected and suggested that the core loop also loosely associates with the same Nef region.

To determine whether a binding synergy also existed between SH3 domains and other Nef ligands, we tested the association between Nef and the C-terminal fragment of the p85 subunit of the PI3 kinase. The C-terminal region, which encompasses the inter-SH2 coiled-coil domain (iSH2), has previously been shown to bind to SF2 Nef [65–67]. However, the structural basis of this association is unknown. Our LAI and SF2 Nef constructs bound to the p85 nSH2–iSH2–cSH2 fragment (nicSH2) with K_ds in the range of 50–150 μM (Figure 2H–K, Table 2). We observed that the affinity tended to decrease with increasing length of the flexible regions and that the presence of R96I/W SH3 domains negatively impacted on the nicSH2 affinity. However, these differences were not significant given the large measurement uncertainties of these low-affinity interactions. We concluded that the presence of the SH3 domains did not markedly increase the binding between Nef and p85 nicSH2 in our assay.

We also probed for a synergy in binding between SH3 domains and the CD4-dileucine motif. A previous NMR study found that the presence of the Hck SH3 domain, which carries an isoleucine on the R position, enhances the affinity of Nef for a CD4-dileucine motif-encompassing peptide by a factor of two (from $K_d \sim$ 1 mM to ~500 μM) [68]. We attempted to reproduce these data using MST and our Nef constructs with and without SH3 domains. However, the CD4 affinities in all cases were below the detection limit of our MST assay (Supplementary Figure S3).

In summary, our data established that SH3 binding to Nef, in particular to Fyn_{R96I}, facilitated the interaction of H1 with the hydrophobic α1–α2 groove of Nef. In turn, binding of H1 also enhanced the affinity of SH3 domains to Nef. The α1–α2 groove is located next to the SH3-binding site, but the two do not overlap; hence,

Biochemical Journal (2021) **478** 1525–1545
https://doi.org/10.1042/BCJ20201002

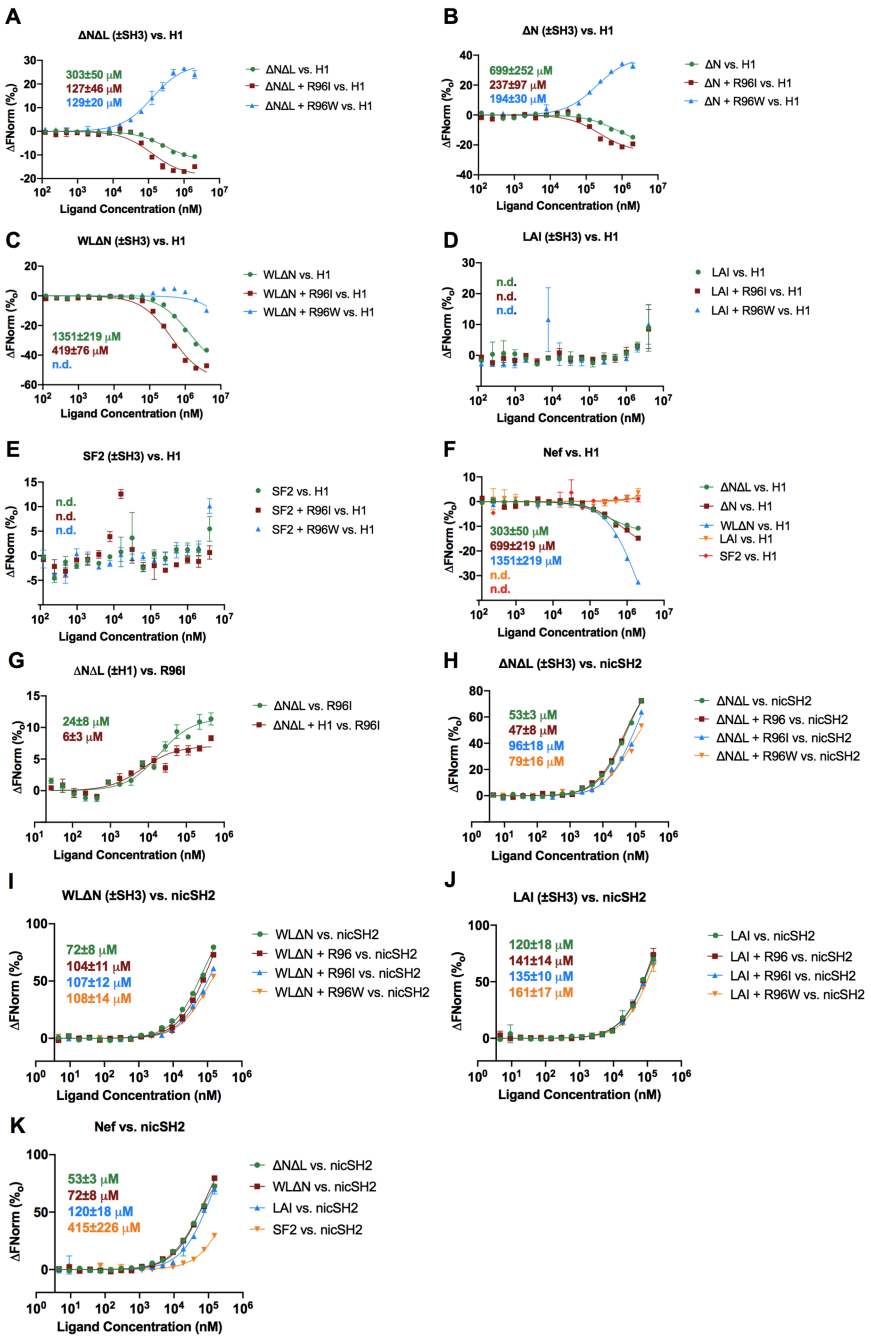

Figure 2. Influence of the flexible regions of Nef on inter- and intramolecular interactions.

Nef was labelled with RED-NHS dye and used at a fixed concentration of 10–50 nM. The + sign indicates a titration series that included measurements where Nef was preincubated with either 50 μM SH3 domains or 1 mM H1 peptide. Error bars represent SD, $n = 3$. Low-affinity titrations where the upper plateau of the sigmoid was missing were only used to draw qualitative conclusions. n.d.: data were measured, but a value for the affinity could not be determined. (**A**) ΔNΔL vs. H1, green; H1 + R96I, brown; or H1 + R96W, blue. (**B**) ΔN vs. H1, green; H1 + R96I, brown; or H1 + R96W, blue. (**C**) WLΔN vs. H1, green; H1 + R96I, brown; or H1 + R96W, blue. (**D**) LAI vs. H1, green; H1 + R96I, brown; or H1 + R96W, blue. (**E**) SF2 vs. H1, green; H1 + R96I, brown; or H1 + R96W, blue. (**F**) ΔNΔL vs. H1, green; ΔN vs. H1, brown; WLΔN vs. H1, blue; LAI vs. H1, orange; or SF2 vs. H1, red. (**G**) ΔNΔL vs. R96I, green or R96I + H1, brown. (**H**) ΔNΔL vs. nicSH2, green; nicSH2 + R96, brown; nicSH2 + R96I, blue; or nicSH2 + R96W, orange. (**I**) WLΔNL vs. nicSH2, green; nicSH2 + R96, brown; nicSH2 + R96I, blue; or nicSH2 + R96W, orange. (**J**) LAI vs. nicSH2, green; nicSH2 + R96, brown; nicSH2 + R96I, blue; or nicSH2 + R96W, orange. (**K**) ΔNΔL vs. nicSH2, green; WLΔN vs. nicSH2, brown; LAI vs. nicSH2, blue; or SF2 vs. nicSH2, orange.

Biochemical Journal (2021) **478** 1525–1545
https://doi.org/10.1042/BCJ20201002

Table 2 Effects of the flexible regions of Nef on inter- and intramolecular interactions

K_d (μM)	H1	H1 + $\underline{Fyn_{R96I}}$	H1 + $\underline{Fyn_{R96W}}$	nicSH2	nicSH2 + $\underline{Fyn_{R96}}$	nicSH2 + $\underline{Fyn_{R96I}}$	nicSH2 + $\underline{Fyn_{R96W}}$	Fyn_{R96I}	Fyn_{R96I} + $\underline{H1}$
ΔNΔL	303 ± 50	127 ± 46	129 ± 20	53 ± 3	47 ± 8	96 ± 18	79 ± 16	24 ± 8	6 ± 3
ΔN	699 ± 252	237 ± 97	194 ± 30	n.d.	n.d.	n.d.	n.d.	n.d.	n.d.
WLΔN	1351 ± 219	419 ± 76	n.d.	72 ± 8	104 ± 11	107 ± 12	108 ± 14	n.d.	n.d.
LAI	n.d.	n.d.	n.d.	120 ± 18	141 ± 14	135 ± 10	161 ± 17	n.d.	n.d.
SF2	n.d.	n.d.	n.d.	n.d.	n.d.	n.d.	n.d.	n.d.	n.d.

MST data were collected at room temperature. Nef was labelled with RED-NHS dye and used at a fixed concentration of 10–50 nM. Preincubated molecules, 50 μM SH3 or 1 mM H1, are underlined.

the binding of one ligand to one site appears to allosterically stabilize the binding site of the other ligand. However, under the conditions used, SH3 binding did not enhance the association of Nef with the p85 C-terminal region or the CD4 dileucine motif. This indicates that the affinity-enhancing effect of SH3 domains does not cover all Nef associations. Moreover, our observation that the Nef core loop and the $W_{57}L$ motif can compete with the H1 motif suggested that these flexible regions can loosely associate with the α1–α2 groove of Nef.

SH3 binding decreases the dynamics of specific Nef regions

Our assays showed that the binding of the SH3 domain increased the affinity of Nef for H1 and *vice versa*, which suggests the existence of allosteric cooperativity. To further investigate this phenomenon, we performed MD simulations comparing the Nef core domain in its apo state (denoted Nef-A) with its Fyn_{R96I}-complexed state (Nef-C). We derived Nef-A and Nef-C from the 2.5 Å resolution crystal structure of LAI $Nef_{54–205,T71R}$ bound to Fyn_{R96I} (PDB ID 1EFN [20]). This crystallographic Nef model lacked residues 54–70 and 149–177, making it akin to the molecule we defined as ΔNΔL. In MD simulations, Nef-C had lower calculated van der Waals and electrostatic energy, and showed decreased overall mobility compared with Nef-A [root mean square fluctuations (RMSF) were 2.52 ± 1.88 Å for Nef-A and 2.16 ± 1.32 Å for Nef-C] (Figure 3A–D), Supplementary Data SDS1.S1), indicating that the SH3 domain stabilized and rigidified Nef. The RMSF differences were greatest in the residues of the N-terminal arm and the core domain loop (Figure 3B). Within the core domain, residues 75–80 showed the strongest stabilization in Nef-C, as expected from their direct interaction with the SH3 domain (Figure 3B,E). However, this SH3-induced stabilization also extended to the underlying residues 111–126, including the C-terminal part of the α2 helix. Additionally, Nef residues 101 to 102 and residue 138 showed fewer fluctuations in the SH3 domain complex (Figure 3B,E). Thus, a large part of the H1 binding site was stabilized by the SH3 domain as was a region that interacts with CD4 [37] and contributes to Nef–Nef crystal contacts (observed in PDB IDs 1EFN, 1AVV, 1AVZ, 4USW, 3REA, and 3D8D) and possibly to dimerization *in vitro* [69] (Figure 3F,G). These results suggested that SH3 binding selectively decreases the dynamics of Nef core regions involved in protein–protein interactions.

Flexible regions can associate in different ways with the Nef α1–α2 groove

Our ITC data showed clear differences in the thermodynamic signatures of the SH3 domain associations with Nef WLΔN compared with the associations of these SH3 domains with other LAI fragments. Our MST data indicated that the binding of H1 to Nef is reduced by the presence of the core loop in the $W_{57}L$ motif and by the additional presence of the N-terminal residues 1–55. Together, these observations suggested that the core loop and the $W_{57}L$ motif compete with H1 for binding to the α1–α2 groove.

Indeed, previous structural analyses found the hydrophobic α1–α2 groove to be occupied by intramolecular protein regions. In NMR studies of a truncated apo-Nef (equivalent to Nef WLΔN plus a deletion of the E_{160}xxxLL endocytosis motif), W57 from the N-terminal extension was found to bind back to the α1–α2 groove (2NEF) [19]. $W_{57}L$ was also associated with the α1–α2 groove, albeit in a different position, in a crystal structure of SF2 Nef bound to an engineered high-affinity SH3 domain (3REA [70]). However, other crystallographic studies of the core domains of HIV-1 and SIV Nef show the α1–α2 groove occupied by the endocytosis motif from the core domain loop of an adjacent molecule in the crystal lattice (PDB IDs: SIV, 5NUH and

Biochemical Journal (2021) **478** 1525–1545
https://doi.org/10.1042/BCJ20201002

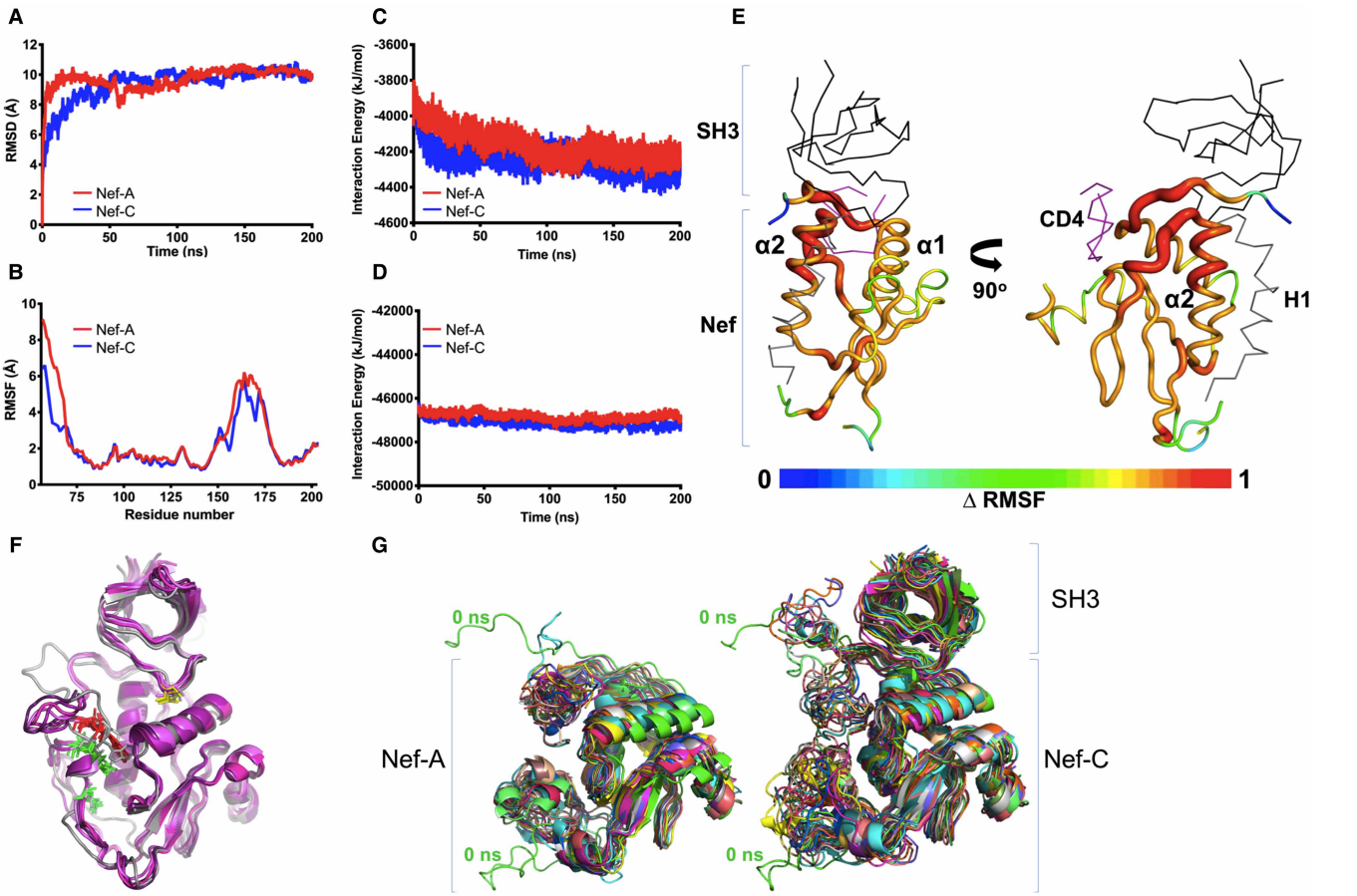

Figure 3. (**A**) Average CαRMSD values as a function of time for Nef-A and Nef-C. (**B**) Average CαRMSF values vs. residue numbers for Nef-A and Nef-C. (**C**) Average Lennard-Jones and (**D**) Coulombic components of the interaction energy monitored over time in Nef-A and Nef-C. (**E**) B-factors showing ΔRMSF between Nef-A and Nef-C from within the 50–200 ns simulation time frame. The gradient scale shows the regions of least and most fluctuations in blue and red, respectively. The SH3 domain is shown in black, CD4 in magenta, and H1 in grey. (**F**) Residual electron density in 1EFN was used to propose a speculative model for concerted backbinding of W_{57}L (red) and E_{160}xxxLL (green) into the α1–α2 groove. The initial model (grey) is superimposed onto structures obtained in MD simulations at 170–200 ns (coloured magenta to dark magenta). I96 is highlighted in yellow. (**G**) Representative snapshots taken every 10 ns for the 3D structure of apo-Nef (*Left*) and the Nef–SH3 complex (*Right*). Nef-A and Nef-C used for structural analysis using molecular dynamics are marked showing stable conformation over the course of simulation.

5NUI; HIV, 3RBB). The binding positions of the endocytosis motifs in HIV and SIV Nef in these crystals were again different [71,72].

Investigating the LAI $Nef_{54\text{-}205,T71R}$–Fyn_{R96I} structure (PDB ID 1EFN), we found strong, continuous residual density in the α1–α2 groove in both Fyn_{R96I}-bound Nef molecules of the asymmetric unit (Supplementary Figure S1). In both molecules of the asymmetric unit, the electron density region closest to W_{57} in the NMR model provided a good fit for a tryptophan side chain whereas the adjacent density fits a leucine side chain. These observations suggest that the W_{57}L motif binds to the α1–α2 groove in these crystal structures (Supplementary Figure S1). In agreement, the electron density for W_{57}L was absent from two LAI Nef LΔN–SH3 complexes crystallized in the same space group as 1EFN, namely, 1AVZ (Nef_{58-205}–Fyn_{R96}) and 4D8D (Nef_{58-205}–Fyn_{R96W} produced for this study; Supplementary Figure S1, Supplementary Table S2).

Assuming this W_{57}L position in the α1–α2 groove, the remaining free electron density in 1EFN cannot be attributed to the residues of the N-terminal region between W_{57} and T_{71} and might correspond to the core loop. A W_{57}L-stabilized association of this loop with the Nef core domain is supported by a relative protection of this loop region from hydrogen exchange [73]. A molecular model for such a 'closed' form, built based on the unattributed residual electron density in 1EFN, was stable in MD runs, which indicates that this

conformation is stereochemically possible (Supplementary Figure S1). Moreover, in MD simulations that started with the core loop and N-terminal arm (residues 57–71) in a dissociated 'open' conformation these flexible elements tended to regroup towards the α1–α2 groove during the simulation (Figure 3A). Hence, our simulations suggested that these flexible residues have a tendency to adapt a 'closed' conformation. Thus, we speculate that in the $W_{57}L$ -containing Nef forms, $W_{57}L$ motif, and the core loop jointly occupy the α1–α2 groove, with the $W_{57}L$ motif directly interacting with the core loop and stabilizing it.

These observations suggest a model that explains our ITC and MST data. In this model, the core loop alone and the $W_{57}L$ motif alone only associate very loosely and dynamically with the α1-α2 groove. When both regions are available this association with the core becomes more stable. However, both can be outcompeted by H1. Further evidence for the capacity of H1 to outcompete other intramolecular regions comes from our survey of the available experimental structures (PDB IDs 6CRI, 4EN2, and 6CM9) (Supplementary Table S3). This survey showed that whenever the H1 motif is present in Nef, it occupies the α1–α2 groove rather than W_{57} or the core loop. In the 3.5 Å crystal structure of full-length LAI bound to Fyn_{R96I} that we determined in this study (PDB ID 7D7S; Supplementary Table S2), the α1–α2 groove was partly occluded by adjacent molecules in the crystal lattice, further supporting the hypothesis that also the H1–core association has a low affinity and can be easily displaced.

Fyn_{r96w} mutation alters the SH3 RT loop hydrogen-bond network

In our ITC titrations, we observed that increasing the hydrophobicity of the SH3 R position from isoleucine to tryptophan resulted in a less favourable entropy contribution, which suggests that the incorporation of tryptophan caused additional loss of degrees of freedom upon binding (Table 1). To compare the RT loop features of apo- and Nef-bound Fyn and Hck SH3 domains, we produced the missing crystal structures of the ligand-free Fyn_{R96I} and Fyn_{R96W} (PDB IDs 3HOF, 3HOH, 3HOI, 6IPY, and 6IPZ; Supplementary Table S1). We observed that the apo Fyn_{R96} and Fyn_{R96I} structures had a similar strong RT loop-rigidifying network formed by six hydrogen bonds (Figure 4). Conversely, the NH group of Fyn_{R96W} disrupted the RT loop hydrogen-bond network and produced an RT loop that was more flexible in its free state. Consequently, the Fyn_{R96W} variant lost more entropy upon fixation of the RT loop in the Nef interface than did Fyn_{R96I}, explaining the less favourable entropy contribution to binding of Fyn_{R96W}. The poor stabilization of the Fyn_{R96W} RT loop is similar to that of Hck SH3, which was previously shown to have a less favourable enthalpy contribution to LAI Nef LΔN binding than those of other SH3 domains, including Fyn_{R96} [27]. Yet, fewer hydrogen bonds are needed to be broken in Fyn_{R96W} upon Nef binding than in Fyn_{R96I} or Fyn_{R96}, which explained the observed greater favourable enthalpy contribution of Fyn_{R96W}.

Nef H1 helix selectively favours short-chain R positions

Our ITC binding studies suggested that the presence of the Nef N-terminal H1 helix has specific effects on SH3 domain binding. The presence of H1 markedly increased the binding of Fyn_{R96I} more than that of Fyn_{R96W} with no significant effects on Fyn_{R96}. Our comparison of all available Nef–SH3 complexes revealed some flexibility in the relative orientation of the SH3 domains with respect to Nef, much of which can be attributed to the crystallographic lattice contacts (Supplementary Data SDS1.S2; Supplementary Figure S1H). However, the R residue position relative to Nef and the canonical P_{72}xxPxR–SH3 interactions are well conserved (Figure 5A). Maintaining these key interactions is possible primarily because of the malleability of the Nef P_{72}xxPxR motif region that, compared with the rest of the Nef core, acts as a buffer for positional differences (Supplementary Figure S1H). We selected the Nef–SH3 complexes that appeared not to be disturbed by the crystallographic lattice and inspected the interactions between the R position and the underlying Nef hydrophobic pocket.

The SH3 R position interacts with the side chains of Nef residues W113 and F90. These side chains have been termed the 'gatekeeper' [72], because they separate the Nef SH3 binding surface from the hydrophobic α1–α2 groove. This groove was observed to bind to H1 and CD4 in previous structural studies [35,68]. Hence, a change in the gatekeeper residue side-chain position resulting from an interaction with the SH3 domain will also affect the shape and size of the hydrophobic groove. The R position of the SH3 domain might therefore influence the ligand interactions of the α1–α2 groove.

We noted that the side-chain position of W113 and, to a lesser extent, F90 changes in response to the different SH3 orientations and different residues in the R position. In cases where the R position is an isoleucine (Hck and Fyn_{R96I}), W113 is rotated towards the SH3 domain and away from the hydrophobic crevice

Biochemical Journal (2021) **478** 1525–1545
https://doi.org/10.1042/BCJ20201002

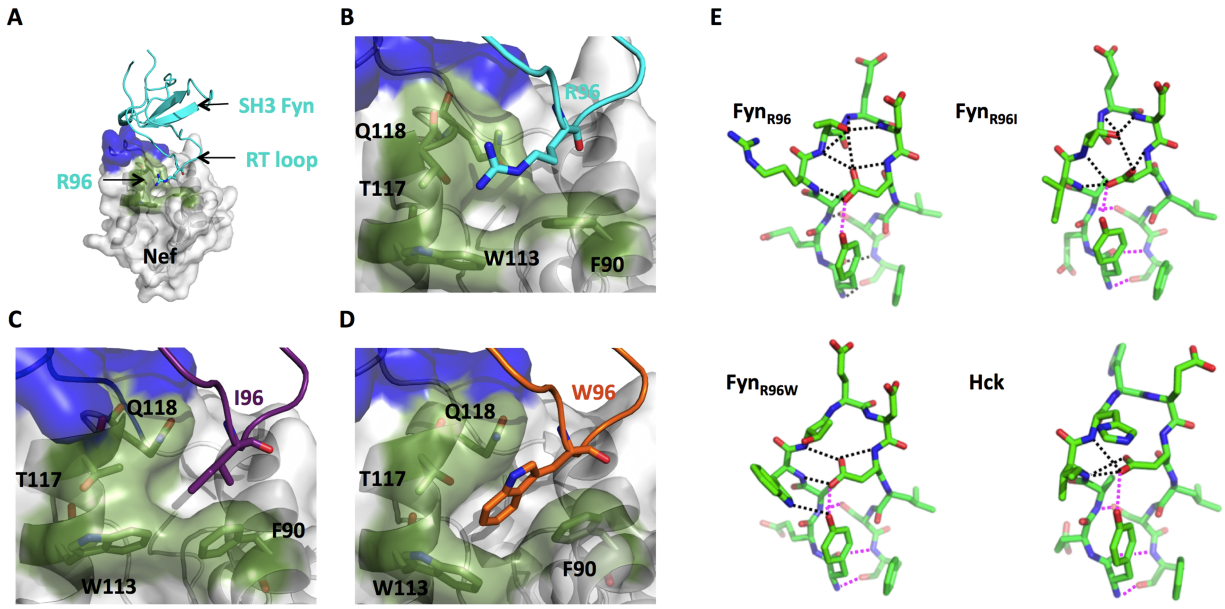

Figure 4. Crystal structures of the Nef core–Fyn SH3 complexes (left) and of the unliganded SH3 domain RT loop (right).
(The linear SH3 binding motif P_{72}xxPxR (blue) and tertiary regions (green) are shown on the surface of Nef. (**A**) Global view of the LΔN–Fyn_{R96} SH3 complex (PDB ID 1AVZ). (**B–D**) Expanded views of the tertiary interaction between SH3 residue 96 and the cognate Nef core pocket. (**B**) LΔN–Fyn_{R96} (PDB ID 1AVZ), (**C**) WLΔN–Fyn_{R96I} (PDB ID 1EFN), and (**D**) LΔN–Fyn_{R96W} (PDB ID 4D8D). (**E**) RT loop hydrogen-bond network of unliganded SH3 domains. In the Nef–SH3 complexes, arginine 77 from the Nef PxxPxR$_{77}$ motif binds to Fyn D100 situated in the center of the RT loop (PDB IDs 1EFN, 1AVZ, 4D8D, and 7D7S). A crystallographic mimicry of this intramolecular salt bridge is frequently observed in unliganded SH3 domains of the Src family. Therefore, only structures without this crystallographic salt bridge were selected. Hydrogen bonds are indicated by dotted lines. Bonds shown in black must be broken upon binding to the Nef core. Hydrogen bonds shown in magenta are preserved in the Nef core–SH3 complex. For Hck SH3, preserved and broken hydrogen bonds were evaluated using a computationally docked LΔN–Hck SH3 complex [22]. SH3 for Fyn_{R96W} but not for Fyn_{R96I}, shows a Hck SH3-like reduced RT-loop hydrogen-bond network (PDB IDs: Hck, 1BU1; Fyn_{R96}, 1SHF; Fyn_{R96I}, 3H0I; Fyn_{R96W}, 6IPZ).

compared with apo-Nef (Figure 5B). Conversely, W113 is pushed into the hydrophobic groove in Fyn_{R96W}-bound Nef structures, whereas W113 adopts an apo side-chain orientation when Nef is in a complex with Fyn_{R96}. Thus, binding to SH3 domains with isoleucine in the R position increases the adjacent α1–α2 groove by 2.3 Å, whereas tryptophan decreases the groove by 0.9 Å; and an arginine leaves it relatively unchanged.

Next, we superimposed the available experimental structures of HIV-1 Nef bound to its N-terminal H1 (EM: PDB IDs 6CM9, 6CRI; X-ray diffraction: 4EN2) with the Nef–SH3 complexes. In the Nef–H1 structures, the malleable N terminal of H1 partly occupies the same Nef region as the R position in the Nef–SH3 complexes. Tryptophan or arginine at the R position clashed more with H1 than isoleucine, suggesting a greater competition of the former with H1. The more stable helical part of H1 fills the α1–α2 groove. In this position, V16 and W13 of H1 are in close contact with W113 (Figure 5C,D). As observed in complexes with Fyn_{R96I} and Hck, an inward-oriented Nef W113 would leave sufficient space for H1, whereas the outward pointing W113 as seen in Fyn_{R96W} complexes would produce mild clashes. From these analyses we concluded that the R position–specific effects of H1 on SH3 binding result from small spatial obstructions that can be direct, or indirect, i.e. mediated by the gatekeeper. These R position–specific effects of H1 are convoluted with the stabilizing effect that H1 has on the Nef core and that non-specifically enhances SH3 interactions.

This model can explain why full-length Nefs discriminate more strongly between Fyn_{R96} and the other two SH3 variants as well as have the highest affinity for Fyn_{R96I}. The additional differences between the SH3 affinities of LAI and SF2 Nef may arise due to the T71R substitution in SF2 Nef, which adds an additional hydrogen bond to the SH3 interaction [28,63]. Our SF2 Nef–Fyn_{R96I} crystal structure did not show any evidence of additional interactions between the flexible regions and the SH3 domain. However, the H1 region of SF2 Nef is

Biochemical Journal (2021) **478** 1525–1545
https://doi.org/10.1042/BCJ20201002

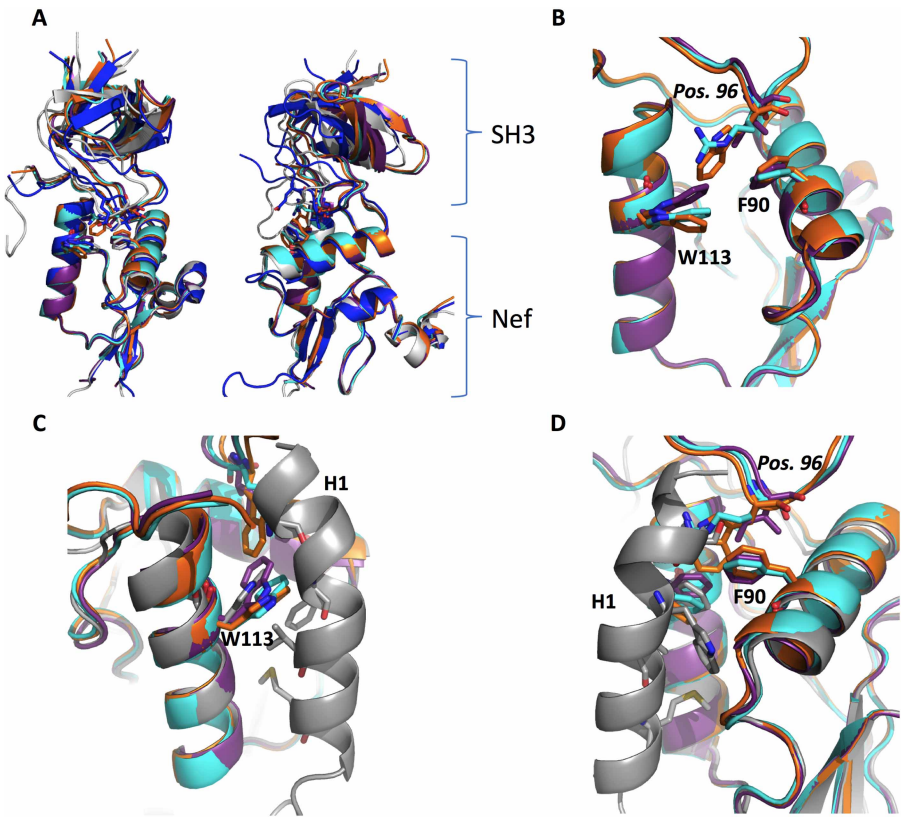

Figure 5. (**A**) Superimposition of Nef structures (PDB ID 1AVZ, cyan; PDB ID 1EFN, purple; PDB ID 4D8D, orange; PDB ID 3RBB, white; PDB ID 4U5W, dark blue). (**B**) Overlay of Nef LAI 'gatekeeper' residues W113/F90 in relation to SH3 position 96 (italics), taken from complexes showing Nef bound to Fyn_{R96} (PDB ID 1AVZ, cyan), Fyn_{R96I} (PDB ID 1EFN, violet purple), and Fyn_{R96W} (PDB ID 4D8D, orange). (**C**–**D**) Overlap of Nef LAI 'gatekeeper' residues bound to H1 (PDB ID 4EN2, grey).

characterized by the duplication of the RAEP motif situated at the C-terminus of H1, and even though this motif has not been predicted to contribute to the intramolecular association, it may have subtle effects on the interaction.

Assessing the prevalence of Nef-like SH3 selectivity based on Fyn_{R96}

In the context of previous work, our analysis of the 'tertiary' association between an SH3 domain and Nef demonstrated that the combination of a linear interaction motif and a folded core domain can create opportunities for synergy and allostery in addition to enhancing affinity and selectivity. Given the promiscuity of SH3–PR motif interactions [74,75], these 'tertiary' features might also be useful for increasing the selectivity in cellular SH3-based signalling.

To investigate whether a Nef-like tertiary SH3 association is a common mode of binding in cellular SH3 associations, we designed a yeast two-hybrid (Y2H) screen. As a high-throughput compatible proxy for this binding mode, we selected cellular proteins that could distinguish between isoleucine and arginine at the R position on the Src family SH3 domains. We used the SH3 domains of Hck, Fyn_{R96}, and Fyn_{R96I} as bait for the Y2H analysis. First, cotransformation of cells with Nef resulted in β-galactosidase production and yeast colony outgrowth on medium lacking uracil with Hck and Fyn_{R96I} as baits but not with Fyn_{R96} (Figure 6A). These results were confirmed using the LacZ and HIS3 reporters for Nef–Hck and Nef–Fyn_{R96}. Because Fyn_{R96I} alone was able to transactivate the LacZ and HIS3 reporters, Fyn_{R96I} could not be used with these reporter systems. Unlike Nef, the Src-associated in mitosis 68 kDa (SAM68) protein interacted with comparable strength with every SH3 domain (Figure 6A), indicating that SAM68 cannot select for the RT-loop R position.

To identify selective cellular binding partners for the SH3 domains of Hck, Fyn_{R96}, and Fyn_{R96I}, we performed Y2H screening using a human fetal library (Figure 6A). To test for a Nef-like differential association,

Biochemical Journal (2021) **478** 1525–1545
https://doi.org/10.1042/BCJ20201002

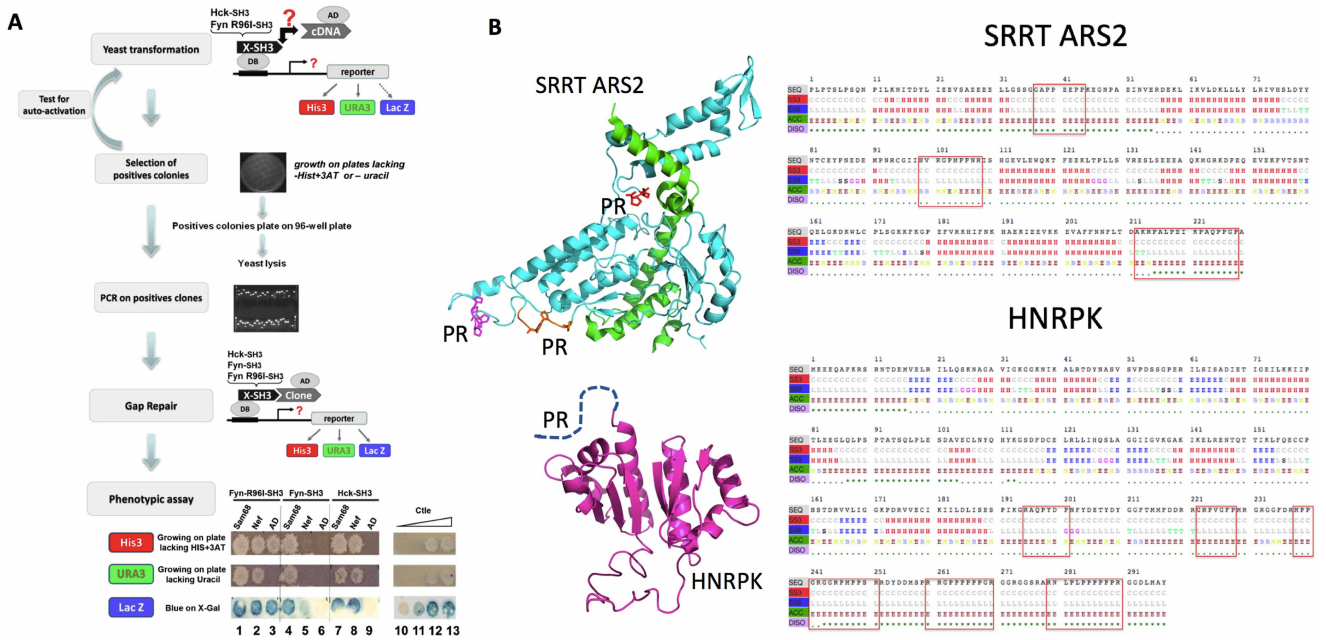

Figure 6. (**A**) Flow chart of the protocol used to identify the proteins displaying differential interactions with the SH3 domains of Hck, Fyn_{R96}, and Fyn_{R96I}. Yeast two-hybrid screens were performed using the SH3 domains of either Hck or Fyn_{R96I}. Remaining positive clones were then tested against the SH3 domains of Hck, Fyn_{R96}, and Fyn_{R96I}. Sometimes, a bait can spontaneously act as a self-activator, so all positive clones were retested by gap repair. We also performed gap repair to screen for the ability of each clone to interact with each SH3 domain. Binding between the two protein partners was determined by staining for β-galactosidase activity (LacZ) and the density of yeast colony outgrowth on a medium lacking histidine (HIS3) or uracil (URA3). The strength of the interactions was evaluated by comparison with signals yielded by various known interactions (lanes 10–13). Clones encoding the HIV-1 Nef and SAM68 proteins were included as controls for differential (Nef; lanes 2, 5, and 8) or similar (SAM68; lanes 1, 4, and 7) binding to the different SH3 domains. The empty plasmid AD encoding Gal4 was used as a negative control (lanes 3, 6, and 9). Because the SH3 domain of Fyn_{R96I} was able to transactivate the LacZ and HIS3 reporters but not URA3, only the URA3 marker was used to evaluate Fyn_{R96I} SH3-mediated interactions. (**B**) *Left panel*: Homology models of SRRT and HNRPK showing the putative proline-rich regions (PR) for binding to SH3 domains. *Right panel*: Prediction of secondary structure, disorder, solvent exposure, and presence of putative SH3-binding PR motifs (boxed). RaptorX DSSP assigns three (SS3) or eight (SS8) secondary structure states as follows: 3_{10}-helix turn (G), α-helix (H), π-helix (I), β-turn (T), β-strand (E), β-bridge (B), high-curvature loop (S), and irregular (L-for eight state or C-for three state). Solvent accessibility is assigned as buried (B), medium exposed (M), and exposed (E). Disorder prediction is annotated by an asterisk (*) to indicate ordered and a period (.) to indicate disordered. Putative SH3-binding PR motifs were identified using ELM.

we performed two coupled serial screens. An initial screen, using the human Hck or Fyn_{R96I} SH3 domain as a bait, yielded 422 and 100 clones, respectively, after gap repair (Supplementary Tables S4, S5). These clones were included in a secondary screen by gap repair against the Hck, Fyn_{R96}, and Fyn_{R96I} SH3 domains, and the clones displaying different strengths of β-galactosidase staining and yeast colony outgrowth on selective medium were selected and sequenced.

We found that only 10 clones — nine from the screen using Hck and three from that using Fyn_{R96I}, representing 2% and 3% of total clones, respectively — had substantially different affinities when Hck and Fyn_{R96I} SH3-mediated interactions were compared with Fyn_{R96}-mediated interactions (Table 3). We then used bioinformatics analysis to identify putative SH3-binding motifs in these sequences and to predict the fragments' secondary structures, solvent exposure, and structural disorder (Supplementary Figure S4).

Five of the ten clones were predicted to be almost entirely disordered, and hence could not produce a tertiary binding site (light red in Table 3). Three clones, ABI1, GFAP and ALIX, possessed a proline-rich motif adjacent to a coiled-coil domain (light blue in Table 3). However, these proline-rich motifs were separated from the folded part by 70, 10 and 20 residues in ABI1, GFAP and ALIX, respectively [46]. We previously reported that ALIX has the capacity to distinguish between arginine and isoleucine in the SH3 R position through a simple linear mechanism rather than a 3D motif [46,59]. Hence, it is likely that also ABI and GFAP achieve this

Table 3 Clones displaying differential interactions with the SH3 domains of Hck, Fyn_{R96}, and Fyn_{R96I}

Clones	Gene ID	Amino acids	Hck-SH3	Fyn_{R96I}-SH3	PxxP	Src binding	References
CTAGE5	4253	81–274	x	x			
Ena/VASP-like	51 466	144–278	x		x	x	[76,77]
FAM59A	64 762	485–872	x		x		[78]
RTN3	10 313	1–266	x		x		
SMN1	6606	199–294		x	x		[79]
Abl-interactor 1	10 006	1–282	x		x	x	[80–82]
ALIX/PDCD6IP	10 015	456–868	x	x	x	x	[46,59]
GFAP	2670	1–308	x		x	x	
SRRT/ARS2	51 593	546–774	x		x		[83]
HNRPK	3190	27–323	x		x	x	[84]

Bold, Italic, Underline refers to our bioinformatics analysis. Bold, entirely disordered proteins; Italic, proteins containing a proline-rich motif close to a folded helical coiled-coil domain separated by a 10–70 amino-acid linker; Underline, proteins with a proline-rich motif close to a globular folded protein core.

selectivity through a linear mechanism. Finally, only two clones, ARS2 and HNRPK, harboured PR motifs within or close to a globular folded protein core (yellow in Table 3). Given this organization, they might provide a 3D environment capable of a tertiary Nef-like SH3 recognition (Figure 6B). We conclude that only a few cellular ligands can select SH3 domains of the Src family according to the same RT-loop residues as used by HIV-1 Nef. In most of these cases, however, this specificity was likely due to a linear binding mode.

Conclusions

Despite lacking catalytic activity, SIV and HIV Nef molecules have a remarkably large range of functions. Just as remarkable is the structural malleability of the flexible regions of Nef, which make up ∼50% of the Nef sequence. We investigated whether the combination of interactions established jointly by Nef's folded core and flexible regions creates synergy and allostery in ligand binding. To overcome the difficulties posed by the structure–function analysis of Nef's flexible regions, we combined structural, biophysical, and computational analyses.

Based on our data, we state that the flexible regions can adopt at least three different conformational states (states I–III; Figure 7). If the N-terminal helix H1 is available, then $W_{57}L$ and the E_{160}xxxLL endocytosis motif are exposed (state I). If H1 is engaged, for example with the membrane, then the combined interaction of W57 and E_{160}xxxLL with the core conceals these motifs (state II). If H1 and $W_{57}L$ are engaged or cleaved, then the E_{160}xxxLL motif only weakly associates with the core (state III).

We demonstrated that there is crosstalk between the flexible regions in the different states and the binding of some, but not all, Nef ligands. We showed that the binding of SH3 domains to the tertiary Nef site affects the binding of H1 to the α1–α2 groove and *vice versa*. Our analysis indicated that this influence results from the combination of a nonspecific dynamic coupling, wherein the binding of one ligand stabilizes the Nef surface for the other ligand, together with a steric interference that is specific for the SH3 R position. This specific interference results from the size of the R position side-chain and its interactions with the Nef gatekeeper residues. Hence, state I binds most tightly to SH3 domains that have a mid-sized hydrophobic isoleucine in the R position, such as Hck, Lyn and possibly Blk (where R is a methionine). States II and III preferred the SH3 domain with a bulky hydrophobic tryptophan in the R position, as in v-Src.

Our analysis corroborated and extended previous findings that the affinity of SH3 domains towards Nef is influenced by the extent of the hydrogen-bond network that stabilizes the RT loop in apo-SH3 [27]. We showed that the incorporation of a tryptophan in Fyn_{R96W} led to a loss of RT-loop hydrogen bonds, making it intrinsically flexible like Hck SH3. We also showed that state I shielded the Nef α1–α2 groove most strongly from other ligands. However, the conformational states and presence of SH3 domains did not have a measurable effect on the binding of the p85 C-terminal fragment to Nef. Our MD simulations explain this selective allostery, at least in part, by showing that the tertiary binding of SH3 domains stabilizes several interaction

Biochemical Journal (2021) **478** 1525–1545
https://doi.org/10.1042/BCJ20201002

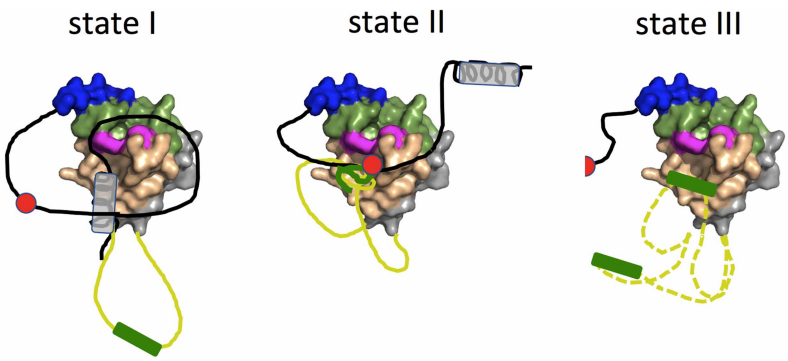

	state I	state II	state III
Preferred SH3 R residue:	isoleucine	tryptophan	tryptophan
$W_{57}L$:	exposed	concealed	exposed/cleaved
E_{160}xxxLL:	exposed	concealed	partly concealed
α1-α2 groove accessibility:	low	moderate	good
H1 binding partner:	Nef	membrane	membrane/cleaved

Figure 7. Proposed conformational states of Nef.

The surface of the Nef core domain is coloured as follows: Blue, P_{72}xxPxR motif; magenta, the gatekeeper residues W113 and F90; green, residues that are engaged in the tertiary SH3 interaction in addition to the gatekeeper residues; and pale brown, the α1–α2 groove. The remaining regions of the Nef core domain are coloured in grey. Flexible regions are indicated as lines. Black line, N-terminal flexible region; grey helix, H1; yellow line, Nef core loop containing the E_{160}xxxLL motif (green); red sphere, $W_{57}L$ motif. The halved red sphere (state III) indicates the presence of only L_{58} after protease cleavage.

surfaces of Nef, including the one used for H1 binding. Thus, our analysis showed that the combination of a tertiary SH3-binding site with large flexible regions can provide an additional level of regulation of ligand binding. *In vivo*, Nef is myristoylated on its N-terminal glycine [21,85]. The presence of this fatty acid chain allows the N-terminal flexible region of Nef (including H1) to associate with charged lipid headgroups of the cell membrane. In the absence of a suitable cellular membrane, the myristoyl is expected to further increase the ways in which the flexible N-terminal arm can associate with the core domain through a myristoyl-switch mechanism [85]. The resulting crosstalk between the conformational states of Nef and its ligands may help to synergize certain subsets of ligands while excluding others with potential functional implications for viral replication.

Based on our findings we make the following predictions and speculations: Due to the mutual reinforcement between the state I conformation and Fyn_{R96I} SH3 interactions, this state may promote the Nef function of activating Hck and Lyn. State II may present a membrane-associated and partly autoinhibited form, in which concealing the $W_{57}L$ and E_{160}xxxLL motifs prevents premature down-regulation in absence of CD4 or other surface receptors, such as CD3. Once a specific ligand binds to the α1–α2 groove, $W_{57}L$ and the endocytosis motif would get exposed to trigger down-regulation of Nef and its cargo. State III would represent the conformation obtained after proteolytic cleavage by the viral protease between W_{57} and L_{58} [62]. Cleaved Nef is predominantly found inside HIV-1 virions [62]. Hence, state III might facilitate tighter packing of Nef molecules within the virion. Upon release into infected cells, state III Nef molecules would remain mostly cytoplasmic, where they easily bind ligands with their poorly concealed α1–α2 groove, while relatively freely displaying their endocytosis motif.

Our findings also raise the possibility that additional subtle allosteric mechanisms are in effect. We noted that the SH3 R position affects the Nef W113 orientation, which, in turn, might affect other ligands. For example, the SH2–SH3 fragments from Fyn or v-Src would not be able to form the same dimeric complex with Nef as Hck SH2–SH3, because of clashes between Fyn R96 and W113, or R96 and Fyn E93 (in Hck the corresponding glutamic acid interacts with R106 of an adjacent Nef molecule in the dimer) [24]. This effect might contribute to the differential outcomes between Nef interactions with Hck and other Src kinases [24,31]. Similarly, the R position of a bound SH3 domain might favour or disfavour specific ligands to the α1–α2 groove. An additional allosteric regulation mechanism might arise from the stabilizing effect of the SH3 domain on selected Nef regions. Thus, SH3 binding could promote certain Nef interactions, including Nef self-

associations. SH3 binding also stabilizes the Nef region involved in CD4 binding. However, the presence of an SH3 domain did not enhance binding of a CD4 peptide in our studies, and the structural models available for this interaction show the proline-rich motif of Nef in a conformation that is incompatible with SH3 binding [37]. Further research is needed to establish which ligands, if any, can bind Nef simultaneously with Src kinases or other SH3-domain containing ligands, such as Tec family kinases [16]. Although our study did not include cell-based functional assays, it provides a new viewpoint through which the different functions and interactions of Nef can be analyzed and better understood.

Considering the versatility and potency of the combination of flexible and folded regions in directing Nef's interactions, we considered whether a Nef-like tertiary interaction is common among cellular SH3 interactions. Our Y2H screen revealed that only very few human SH3-binding proteins distinguish SH3 domains according to the same RT-loop residue as Nef. Our bioinformatics analysis and the experimentally established example of ALIX show that the RT-loop selectivity of these cellular proteins does not necessarily require a Nef-like tertiary interaction but can be obtained through a linear peptide-like binding mode. Although our study could not rule out the presence of supplementary SH3 associations in general, the results imply that a Nef-like tertiary, and possibly allosterically active, SH3 binding mode is not common among cellular proteins. Hence, this binding mode appears to be a *de novo* adaptation that is specific to this viral protein. It is possible that Nef's affinity and selectivity characteristics are intrinsically unsuitable for mediating SH3 binding in cellular signalling. The tertiary recognition mode of Nef results in strong SH3 binding, which not only activates Src kinases that contain a favoured isoleucine in the R position, such as Hck or Lyn, but also interferes with the function of those with less favourable R residues, such as Lck, which has a serine, or Fyn and Src, which have an arginine [30,31,86,87]. The Nef–SH3 domain binding mode may therefore be too strong to be widely used in cells where it might disrupt several Src kinases. The uniqueness of the tertiary SH3-binding site of Nef supports the identification of this site as a selective antiviral drug target without an apparent risk of crossreactions with other cellular proteins [88].

Data Availability

All crystallographic data are deposited in the Protein Data Bank (Fyn SH3 domain mutants, 3H0F, 3H0H, 3H0I, 6IPY, and 6IPZ; Nef–Fyn complexes, 4D8D and 7D7S). Additionally, unmerged crystallographic data are available as PDB ID 7D7S at https://doi.org/10.25781/KAUST-8CV15.

Competing Interests

The authors declare that there are no competing interests associated with the manuscript.

Funding

This research was supported by funding from King Abdullah University of Science and Technology through the baseline fund and award no. FCC/1/1976-25 from the Office of Sponsored Research. For computer time, this research used the resources of the Supercomputing Laboratory at King Abdullah University of Science & Technology (KAUST) in Thuwal, Saudi Arabia. This work was supported by the Centre National de la Recherche Scientifique; the Institut National de la Santé et de la Recherche Médicale; the Agence Nationale de Recherche sur le SIDA et les hépatites virales; the Ministry of Science and Technology, China [grant numbers 2007CB914304 and 2006AA02A313]; the National Natural Science Foundation of China [grant numbers 30800181 and 30625011]; the Research Foundation Flanders; the Concerted Action Program of the Katholieke Universiteit Leuven; and the National Institutes of Health (MD Anderson's Cancer Center Support) [grant number CA016672]. S.O. and A.L. were fellows of the ANRS, and X.S. was a fellow of the 'Ambassade de France en Chine.'

CRediT Contribution

Stefan Arold: Conceptualization, Formal analysis, Supervision, Funding acquisition, Validation, Investigation, Visualization, Writing — original draft, Project administration, Writing — review and editing. **Abdullah M. Aldehaiman:** Conceptualization, Data curation, Formal analysis, Supervision, Validation, Investigation, Writing — review and editing. **Afaque A. Momin:** Conceptualization, Data curation, Formal analysis, Validation, Investigation, Writing — original draft, Writing — review and editing. **Audrey Restouin:** Data curation, Validation, Investigation. **Luyao Wang:** Formal analysis, Investigation. **Xiaoli Shi:** Formal analysis, Investigation, Visualization. **Safia Aljedani:** Investigation. **Sandrine Opi:** Validation, Investigation, Visualization. **Adrien Lugari:** Investigation, Visualization, Writing — original draft. **Umar F. Shahul Hameed:** Supervision, Investigation. **Luc**

Biochemical Journal (2021) **478** 1525–1545
https://doi.org/10.1042/BCJ20201002

Ponchon: Investigation. **Xavier Morelli:** Conceptualization, Supervision, Funding acquisition, Investigation, Writing — original draft, Writing — review and editing. **Mingdong Huang:** Conceptualization, Supervision, Funding acquisition, Validation, Writing — review and editing. **Christian Dumas:** Conceptualization, Supervision, Validation, Investigation, Writing — original draft, Writing — review and editing. **Yves Collette:** Conceptualization, Supervision, Funding acquisition, Validation, Investigation, Visualization, Writing — original draft, Writing — review and editing.

Acknowledgements

We acknowledge SOLEIL for the provision of synchrotron radiation facilities. We also thank L. Chavas, P. Legrand, S. Sirigu, and P. Montaville for their assistance with beamline PROXIMA 1 and G. Fox, M. Savko, and B. Shepard with PROXIMA 2A. We also thank M-P. Struband and M-T. Augé-Sénégas for the initial cloning of some of the Fyn_{R96I} and Fyn_{R96W} mutants. We thank M. Geyer for providing the expression construct of Nef SF2. We acknowledge the staff at ESRF beamline BM30, Grenoble, France, for their assistance with crystallographic data collection. We also thank the KAUST Supercomputing Laboratory for their assistance with computational resources for molecular dynamics simulations using the IBEX cluster.

Abbreviations

HIS3, histidine; ITC, isothermal titration calorimetry; MST, microscale thermophoresis; PDB, Protein Data Bank; PR, proline-rich regions; RMSF, root mean square fluctuations; SAM68, Src-associated in mitosis 68 kDa; URA3, uracil.

References

1 Arold, S.T. and Baur, A.S. (2001) Dynamic Nef and Nef dynamics: how structure could explain the complex activities of this small HIV protein. *Trends Biochem. Sci.* **26**, 356–363 https://doi.org/10.1016/S0968-0004(01)01846-1
2 Kirchhoff, F., Schindler, M., Specht, A., Arhel, N. and Münch, J. (2008) Role of Nef in primate lentiviral immunopathogenesis. *Cell. Mol. Life Sci.* **65**, 2621–2636 https://doi.org/10.1007/s00018-008-8094-2
3 Kestler, H.W., Ringler, D.J., Mori, K., Panicali, D.L., Sehgal, P.K., Daniel, M.D. et al. (1991) Importance of the nef gene for maintenance of high virus loads and for development of AIDS. *Cell* **65**, 651–662 https://doi.org/10.1016/0092-8674(91)90097-I
4 Kirchhoff, F., Greenough, T.C., Brettler, D.B., Sullivan, J.L. and Desrosiers, R.C. (1995) Absence of intact nef sequences in a long-Term survivor with nonprogressive HIV-1 infection. *N. Engl. J. Med.* **332**, 228–232 https://doi.org/10.1056/NEJM199501263320405
5 Deacon, N.J., Tsykin, A., Solomon, A., Smith, K., Ludford-Menting, M., Hooker, D.J. et al. (1995) Genomic structure of an attenuated quasi species of HIV-1 from a blood transfusion donor and recipients. *Science* **270**, 988–991 https://doi.org/10.1126/science.270.5238.988
6 Pereira, E.A. and da Silva, L.L.P. (2016) HIV-1 Nef: taking control of protein trafficking. *Traffic* **17**, 976–996 https://doi.org/10.1111/tra.12412
7 Buffalo, C.Z., Iwamoto, Y., Hurley, J.H. and Ren, X. (2019) How HIV Nef proteins hijack membrane traffic To promote infection. *J. Virol.* **93**, e01322-19 https://doi.org/10.1128/JVI.01322-19
8 Lama, J. and Ware, C.F. (2000) Human immunodeficiency virus type 1 Nef mediates sustained membrane expression of tumor necrosis factor and the related cytokine LIGHT on activated T cells. *J. Virol.* **74**, 9396–9402 https://doi.org/10.1128/JVI.74.20.9396-9402.2000
9 Sol-Foulon, N., Moris, A., Nobile, C., Boccaccio, C., Engering, A., Abastado, J.-P. et al. (2002) HIV-1 Nef-induced upregulation of DC-SIGN in dendritic cells promotes lymphocyte clustering and viral spread. *Immunity* **16**, 145–155 https://doi.org/10.1016/S1074-7613(02)00260-1
10 Schrager, J.A. and Marsh, J.W. (1999) HIV-1 Nef increases T cell activation in a stimulus-dependent manner. *Proc. Natl Acad. Sci. U.S.A.* **96**, 8167–8172 https://doi.org/10.1073/pnas.96.14.8167
11 Markle, T.J., Philip, M. and Brockman, M.A. (2013) HIV-1 Nef and T-cell activation: a history of contradictions. *Future Virol.* **8**, 10.2217/fvl.13.20 https://doi.org/10.2217/fvl.13.20
12 Swingler, S., Mann, A., Jacqué, J., Brichacek, B., Sasseville, V.G., Williams, K. et al. (1999) HIV-1 Nef mediates lymphocyte chemotaxis and activation by infected macrophages. *Nat. Med.* **5**, 997–103 https://doi.org/10.1038/12433
13 Arora, V.K., Molina, R.P., Foster, J.L., Blakemore, J.L., Chernoff, J., Fredericksen, B.L. et al. (2000) Lentivirus Nef specifically activates Pak2. *J. Virol.* **74**, 11081–7 https://doi.org/10.1128/JVI.74.23.11081-11087.2000
14 Renkema, G.H., Manninen, A., Mann, D.A., Harris, M. and Saksela, K. (1999) Identification of the Nef-associated kinase as p21-activated kinase 2. *Curr. Biol.* **9**, 1407–1411 https://doi.org/10.1016/S0960-9822(00)80086-X
15 Briggs, S.D., Sharkey, M., Stevenson, M. and Smithgall, T.E. (1997) SH3-mediated hck tyrosine kinase activation and fibroblast transformation by the Nef protein of HIV-1. *J. Biol. Chem.* **272**, 17899–17902 https://doi.org/10.1074/jbc.272.29.17899
16 Tarafdar, S., Poe, J.A. and Smithgall, T.E. (2014) The accessory factor Nef links HIV-1 to Tec/Btk kinases in an Src homology 3 domain-dependent manner. *J. Biol. Chem.* **289**, 15718–15728 https://doi.org/10.1074/jbc.M114.572099
17 Emert-Sedlak, L.A., Narute, P., Shu, S.T., Poe, J.A., Shi, H., Yanamala, N. et al. (2013) Effector kinase coupling enables high-throughput screens for direct HIV-1 Nef antagonists with antiretroviral activity. *Chem. Biol.* **20**, 82–91 https://doi.org/10.1016/j.chembiol.2012.11.005
18 Wolf, D., Witte, V., Laffert, B., Blume, K., Stromer, E., Trapp, S. et al. (2001) HIV-1 Nef associated PAK and PI3-Kinases stimulate Akt-independent Bad-phosphorylation to induce anti-apoptotic signals. *Nat. Med.* **7**, 1217–1224 https://doi.org/10.1038/nm1101-1217
19 Grzesiek, S., Bax, A., Hu, J.S., Kaufman, J., Palmer, I., Stahl, S.J. et al. (1997) Refined solution structure and backbone dynamics of HIV-1 Nef. *Protein Sci.* **6**, 1248–1263 https://doi.org/10.1002/pro.5560060613

20 Lee, C.-H., Saksela, K., Mirza, U.A., Chait, B.T. and Kuriyan, J. (1996) Crystal structure of the conserved core of HIV-1 Nef complexed with a Src family SH3 domain. *Cell* **85**, 931–942 https://doi.org/10.1016/S0092-8674(00)81276-3
21 Geyer, M., Munte, C.E., Schorr, J., Kellner, R. and Kalbitzer, H.R. (1999) Structure of the anchor-domain of myristoylated and non-myristoylated HIV-1 Nef protein. *J. Mol. Biol.* **289**, 123–138 https://doi.org/10.1006/jmbi.1999.2740
22 Arold, S., Franken, P., Strub, M.P., Hoh, F., Benichou, S., Benarous, R. et al. (1997) The crystal structure of HIV-1 Nef protein bound to the Fyn kinase SH3 domain suggests a role for this complex in altered T cell receptor signaling. *Structure* **5**, 1361–1372 https://doi.org/10.1016/S0969-2126(97)00286-4
23 Bentham, M., Mazaleyrat, S. and Harris, M. (2006) Role of myristoylation and N-terminal basic residues in membrane association of the human immunodeficiency virus type 1 Nef protein. *J. Gen. Virol.* **87**, 563–571 https://doi.org/10.1099/vir.0.81200-0
24 Alvarado, J.J., Tarafdar, S., Yeh, J.I. and Smithgall, T.E. (2014) Interaction with the Src homology (SH3-SH2) region of the Src-family kinase Hck structures the HIV-1 Nef dimer for kinase activation and effector recruitment. *J. Biol. Chem.* **289**, 28539–28553 https://doi.org/10.1074/jbc.M114.600031
25 Lee, C.H., Leung, B., Lemmon, M.A., Zheng, J., Cowburn, D., Kuriyan, J. et al. (1995) A single amino acid in the SH3 domain of Hck determines its high affinity and specificity in binding to HIV-1 Nef protein. *EMBO J.* **14**, 5006–5015 https://doi.org/10.1002/j.1460-2075.1995.tb00183.x
26 Collette, Y., Arold, S., Picard, C., Janvier, K., Benichou, S., Benarous, R. et al. (2000) HIV-2 and SIV Nef proteins target different Src family SH3 domains than does HIV-1 Nef because of a triple amino acid substitution. *J. Biol. Chem.* **275**, 4171–4176 https://doi.org/10.1074/jbc.275.6.4171
27 Arold, S., O'Brien, R., Franken, P., Strub, M.-P., Hoh, F., Dumas, C. et al. (1998) RT loop flexibility enhances the specificity of Src family SH3 domains for HIV-1 Nef. *Biochemistry* **37**, 14683–14691 https://doi.org/10.1021/bi980989q
28 Moarefi, I., LaFevre-Bernt, M., Sicheri, F., Huse, M., Lee, C.H., Kuriyan, J. et al. (1997) Activation of the Src-family tyrosine kinase Hck by SH3 domain displacement. *Nature* **385**, 650–653 https://doi.org/10.1038/385650a0
29 Lerner, E.C. and Smithgall, T.E. (2002) SH3-dependent stimulation of Src-family kinase autophosphorylation without tail release from the SH2 domain in vivo. *Nat. Struct. Biol.* **9**, 365–369 https://doi.org/10.1038/nsb782
30 Trible, R.P., Emert-Sedlak, L. and Smithgall, T.E. (2006) HIV-1 Nef selectively activates Src family kinases Hck, Lyn, and c-Src through direct SH3 domain interaction. *J. Biol. Chem.* **281**, 27029–27038 https://doi.org/10.1074/jbc.M601128200
31 Briggs, S.D., Lerner, E.C. and Smithgall, T.E. (2000) Affinity of Src family kinase SH3 domains for HIV Nef in vitro does not predict kinase activation by Nef in vivo. *Biochemistry* **39**, 489–495 https://doi.org/10.1021/bi992504j
32 Hung, C.-H., Thomas, L., Ruby, C.E., Atkins, K.M., Morris, N.P., Knight, Z.A. et al. (2007) HIV-1 Nef assembles a Src family kinase-ZAP-70/Syk-PI3K cascade to downregulate cell-Surface MHC-I. *Cell Host Microbe* **1**, 121–133 https://doi.org/10.1016/j.chom.2007.03.004
33 Lee, J.-H., Ostalecki, C., Zhao, Z., Kesti, T., Bruns, H., Simon, B. et al. (2018) HIV activates the tyrosine kinase Hck to secrete ADAM protease-Containing extracellular vesicles. *EBioMedicine* **28**, 151–161 https://doi.org/10.1016/j.ebiom.2018.01.004
34 Ren, X., Park, S.Y., Bonifacino, J.S. and Hurley, J.H. (2014) How HIV-1 Nef hijacks the AP-2 clathrin adaptor to downregulate CD4. *eLife* **3**, e01754 https://doi.org/10.7554/eLife.01754
35 Morris, K.L., Buffalo, C.Z., Stürzel, C.M., Heusinger, E., Kirchhoff, F., Ren, X. et al. (2018) HIV-1 Nefs are cargo-sensitive AP-1 trimerization switches in tetherin downregulation. *Cell* **174**, 659–671.e14 https://doi.org/10.1016/j.cell.2018.07.004
36 Jia, X., Singh, R., Homann, S., Yang, H., Guatelli, J. and Xiong, Y. (2012) Structural basis of evasion of cellular adaptive immunity by HIV-1 Nef. *Nat. Struct. Mol. Biol.* **19**, 701–706 https://doi.org/10.1038/nsmb.2328
37 Kwon, Y., Kaake, R.M., Echeverria, I., Suarez, M., Karimian Shamsabadi, M., Stoneham, C. et al. (2020) Structural basis of CD4 downregulation by HIV-1 Nef. *Nat. Struct. Mol. Biol.* **27**, 822–828 https://doi.org/10.1038/s41594-020-0463-z
38 Bacterial Expression Vectors - DNA2.0 [Internet]. 2012 [cited 2021 Mar 16]. Available from: https://web.archive.org/web/20120320183542/https://www.dna20.com/pJexpress.php
39 Leslie, A.G.W. (1992) Recent changes to the MOSFLM package for processing film and image plate data. CCP4 and ESF-EACMB Newsletter on Protein Crystallography
40 Collaborative Computational Project, Number 4. (1994) The CCP4 suite: programs for protein crystallography. *Acta Crystallogr. D Biol. Crystallogr.* **50**, 760–763 https://doi.org/10.1107/S0907444994003112
41 Hungler, A., Momin, A., Diederichs, K. and Arold, S.T. (2016) Contaminer and contaBase: a webserver and database for early identification of unwantedly crystallized protein contaminants. *J. Appl. Cryst.* **49**, 2252–2258 https://doi.org/10.1107/S1600576716014965
42 Vagin, A. and Teplyakov, A. (1997) MOLREP: an automated program for molecular replacement. *J. Appl. Cryst.* **30**, 1022–1025 https://doi.org/10.1107/S0021889897006766
43 Noble, M.E., Musacchio, A., Saraste, M., Courtneidge, S.A. and Wierenga, R.K. (1993) Crystal structure of the SH3 domain in human Fyn; comparison of the three-dimensional structures of SH3 domains in tyrosine kinases and spectrin. *EMBO J.* **12**, 2617–2624 https://doi.org/10.1002/j.1460-2075.1993.tb05922.x
44 Murshudov, G.N., Vagin, A.A. and Dodson, E.J. (1997) Refinement of macromolecular structures by the maximum-likelihood method. *Acta Crystallogr. D Biol Crystallogr.* **53**, 240–255 https://doi.org/10.1107/S0907444996012255
45 Emsley, P. and Cowtan, K. (2004) Coot: model-building tools for molecular graphics. *Acta Crystallogr. D Biol Crystallogr.* **60**, 2126–2132 https://doi.org/10.1107/S0907444904019158
46 Shi, X., Opi, S., Lugari, A., Restouin, A., Coursindel, T., Parrot, I. et al. (2010) Identification and biophysical assessment of the molecular recognition mechanisms between the human haemopoietic cell kinase Src homology domain 3 and ALG-2-interacting protein X. *Biochem. J.* **431**, 93–102 https://doi.org/10.1042/BJ20100314
47 Vagin, A. and Lebedev, A. (2015) MoRDa, an automatic molecular replacement pipeline. *Acta Crystallogr. Sect. A Found. Adv.* **71**, s19 https://doi.org/10.1107/S2053273315099672
48 Cowtan, K. (2006) The Buccaneer software for automated model building. 1. Tracing protein chains. *Acta Crystallogr. D Biol Crystallogr.* **62**, 1002–1011 https://doi.org/10.1107/S0907444906022116
49 Murshudov, G.N., Skubák, P., Lebedev, A.A., Pannu, N.S., Steiner, R.A., Nicholls, R.A. et al. (2011) REFMAC5 for the refinement of macromolecular crystal structures. *Acta Crystallogr. D Biol Crystallogr.* **67**, 355–367 https://doi.org/10.1107/S0907444911001314

Biochemical Journal (2021) **478** 1525–1545
https://doi.org/10.1042/BCJ20201002

50 DiMaio, F., Echols, N., Headd, J.J., Terwilliger, T.C., Adams, P.D. and Baker, D. (2013) Improved low-resolution crystallographic refinement with Phenix and Rosetta. *Nat. Methods* **10**, 1102–1104 https://doi.org/10.1038/nmeth.2648

51 Vonrhein, C., Tickle, I.J., Flensburg, C., Keller, P., Paciorek, W., Sharff, A. et al. (2018) Advances in automated data analysis and processing within autoPROC, combined with improved characterisation, mitigation and visualisation of the anisotropy of diffraction limits using STARANISO. *Acta Crystallogr. Sect. A Found. Adv.* **74**, a360 https://doi.org/10.1107/S010876731809640X

52 Kovalevskiy, O., Nicholls, R.A. and Murshudov, G.N. (2016) Automated refinement of macromolecular structures at low resolution using prior information. *Acta Crystallogr. D Biol Crystallogr.* **72**, 1149–1161 https://doi.org/10.1107/S2059798316014534

53 Abraham, M.J., Murtola, T., Schulz, R., Páll, S., Smith, J.C., Hess, B. et al. (2015) GROMACS: high performance molecular simulations through multi-level parallelism from laptops to supercomputers. *SoftwareX* **1–2**, 19–25 https://doi.org/10.1016/j.softx.2015.06.001

54 Maier, J.A., Martinez, C., Kasavajhala, K., Wickstrom, L., Hauser, K.E. and Simmerling, C. (2015) ff14SB: improving the accuracy of protein side chain and backbone parameters from ff99SB. *J. Chem. Theory Comput.* **11**, 3696–3713 https://doi.org/10.1021/acs.jctc.5b00255

55 Bussi, G., Donadio, D. and Parrinello, M. (2007) Canonical sampling through velocity rescaling. *J. Chem. Phys.* **126**, 014101 https://doi.org/10.1063/1.2408420

56 Parrinello, M. and Rahman, A. (1981) Polymorphic transitions in single crystals: a new molecular dynamics method. *J. Appl. Phys.* **52**, 7182–7190 https://doi.org/10.1063/1.328693

57 Essmann, U., Perera, L., Berkowitz, M.L., Darden, T., Lee, H. and Pedersen, L.G. (1995) A smooth particle mesh ewald method. *J. Chem. Phys.* **103**, 8577–8593 https://doi.org/10.1063/1.470117

58 Hess, B., Bekker, H., Berendsen, H.J.C. and Fraaije, J.G.E.M. (1997) LINCS: a linear constraint solver for molecular simulations. *J. Comput. Chem.* **18**, 1463–1472 https://doi.org/10.1002/(SICI)1096-987X(199709)18:12<1463::AID-JCC4>3.0.CO;2-H

59 Shi, X., Betzi, S., Lugari, A., Opi, S., Restouin, A., Parrot, I. et al. (2012) Structural recognition mechanisms between human Src homology domain 3 (SH3) and ALG-2-interacting protein X (Alix). *FEBS Lett.* **586**, 1759–1764 https://doi.org/10.1016/j.febslet.2012.05.017

60 Källberg, M., Wang, H., Wang, S., Peng, J., Wang, Z., Lu, H. et al. (2012) Template-based protein structure modeling using the raptorX web server. *Nat. Protoc.* **7**, 1511–1522 https://doi.org/10.1038/nprot.2012.085

61 Kumar, M., Gouw, M., Michael, S., Sámano-Sánchez, H., Pancsa, R., Glavina, J. et al. (2020) ELM—the eukaryotic linear motif resource in 2020. *Nucleic Acids Res.* **48**, D296–D306 https://doi.org/10.1093/nar/gkz1030

62 Chen, Y.-L., Trono, D. and Camaur, D. (1998) The proteolytic cleavage of human immunodeficiency virus type 1 Nef does not correlate with its ability To stimulate virion infectivity. *J. Virol.* **72**, 3178–3184 https://doi.org/10.1128/JVI.72.4.3178-3184.1998

63 Saksela, K., Cheng, G. and Baltimore, D. (1995) Proline-rich (PxxP) motifs in HIV-1 Nef bind to SH3 domains of a subset of Src kinases and are required for the enhanced growth of Nef+ viruses but not for down-regulation of CD4. *EMBO J.* **14**, 484–491 https://doi.org/10.1002/j.1460-2075.1995.tb07024.x

64 Chodera, J.D. and Mobley, D.L. (2013) Entropy-Enthalpy compensation: role and ramifications in biomolecular ligand recognition and design. *Annu. Rev. Biophys.* **42**, 121–142 https://doi.org/10.1146/annurev-biophys-083012-130318

65 Linnemann, T., Zheng, Y.-H., Mandic, R. and Matija Peterlin, B. (2002) Interaction between Nef and phosphatidylinositol-3-Kinase leads to activation of p21-Activated kinase and increased production of HIV. *Virology* **294**, 246–255 https://doi.org/10.1006/viro.2002.1365

66 Graziani, A., Galimi, F., Medico, E., Cottone, E., Gramaglia, D., Boccaccio, C. et al. (1996) The HIV-1 Nef protein interferes with phosphatidylinositol 3-kinase activation 1. *J. Biol. Chem.* **271**, 6590–6593 https://doi.org/10.1074/jbc.271.12.6590

67 Kim, Y.-H., Chang, S.H., Kwon, J.H. and Rhee, S.S. (1999) HIV-1 Nef plays an essential role in two independent processes in CD4 down-regulation: dissociation of the CD4–p56lck complex and targeting of CD4 to lysosomes. *Virology* **257**, 208–219 https://doi.org/10.1006/viro.1999.9642

68 Grzesiek, S., Stahl, S.J., Wingfield, P.T. and Bax, A. (1996) The CD4 determinant for downregulation by HIV-1 Nef directly binds to Nef. mapping of the Nef binding surface by NMR. *Biochemistry* **35**, 10256–10261 https://doi.org/10.1021/bi9611164

69 Franken, P., Arold, S., Padilla, A., Hoh, E., Strub, M.P., Boyer, M. et al. (1997) HIV-1 Nef protein: purification, crystallizations, and preliminary X-ray diffraction studies. *Protein Sci.* **6**, 2681–2683 https://doi.org/10.1002/pro.5560061227

70 Breuer, S., Schievink, S.I., Schulte, A., Blankenfeldt, W., Fackler, O.T. and Geyer, M. (2011) Molecular design, functional characterization and structural basis of a protein inhibitor against the HIV-1 pathogenicity factor Nef. *PLoS ONE* **6**, e20033 https://doi.org/10.1371/journal.pone.0020033

71 Manrique, S., Sauter, D., Horenkamp, F.A., Lülf, S., Yu, H., Hotter, D. et al. (2017) Endocytic sorting motif interactions involved in Nef-mediated downmodulation of CD4 and CD3. *Nat. Commun.* **8**, 442 https://doi.org/10.1038/s41467-017-00481-z

72 Horenkamp, F.A., Breuer, S., Schulte, A., Lülf, S., Weyand, M., Saksela, K. et al. (2011) Conformation of the dileucine-based sorting motif in HIV-1 Nef revealed by intermolecular domain assembly. *Traffic* **12**, 867–877 https://doi.org/10.1111/j.1600-0854.2011.01205.x

73 Hochrein, J.M., Wales, T.E., Lerner, E.C., Schiavone, A.P., Smithgall, T.E. and Engen, J.R. (2006) Conformational features of the full-Length HIV and SIV Nef proteins determined by mass spectrometry. *Biochemistry* **45**, 7733–7739 https://doi.org/10.1021/bi060438x

74 Ladbury, J.E. and Arold, S.T. (2012) Noise in cellular signaling pathways: causes and effects. *Trends Biochem. Sci.* **37**, 173–178 https://doi.org/10.1016/j.tibs.2012.01.001

75 Ladbury, J.E. and Arold, S. (2000) Searching for specificity in SH domains. *Chem. Biol.* **7**, R3–R8 https://doi.org/10.1016/S1074-5521(00)00067-3

76 Reinhard, M., Jarchau, T. and Walter, U. (2001) Actin-based motility: stop and go with Ena/VASP proteins. *Trends Biochem. Sci.* **26**, 243–249 https://doi.org/10.1016/S0968-0004(00)01785-0

77 Kwiatkowski, A.V., Gertler, F.B. and Loureiro, J.J. (2003) Function and regulation of Ena/VASP proteins. *Trends Cell Biol.* **13**, 386–392 https://doi.org/10.1016/S0962-8924(03)00130-2

78 Tashiro, K., Tsunematsu, T., Okubo, H., Ohta, T., Sano, E., Yamauchi, E. et al. (2009) GAREM, a novel adaptor protein for growth factor receptor-bound protein 2, contributes to cellular transformation through the activation of extracellular signal-regulated kinase signaling. *J. Biol. Chem.* **284**, 20206–20214 https://doi.org/10.1074/jbc.M109.021139

79 Kurihara, N., Menaa, C., Maeda, H., Haile, D.J. and Reddy, S.V. (2001) Osteoclast-stimulating factor interacts with the spinal muscular atrophy gene product to stimulate osteoclast formation. *J. Biol. Chem.* **276**, 41035–9 https://doi.org/10.1074/jbc.M100233200

80 Shi, Y., Alin, K. and Goff, S.P. (1995) Abl-interactor-1, a novel SH3 protein binding to the carboxy-terminal portion of the Abl protein, suppresses v-abl transforming activity. *Genes Dev.* **9**, 2583–2597 https://doi.org/10.1101/gad.9.21.2583

81 Rickles, R.J., Botfield, M.C., Weng, Z., Taylor, J.A., Green, O.M., Brugge, J.S. et al. (1994) Identification of Src, Fyn, Lyn, PI3K and Abl SH3 domain ligands using phage display libraries. *EMBO J.* **13**, 5598–5604 https://doi.org/10.1002/j.1460-2075.1994.tb06897.x
82 Sparks, A.B., Rider, J.E., Hoffman, N.G., Fowlkes, D.M., Quillam, L.A. and Kay, B.K. (1996) Distinct ligand preferences of Src homology 3 domains from Src, Yes, Abl, Cortactin, p53bp2, PLCgamma, Crk, and Grb2. *Proc. Natl Acad. Sci. U.S.A.* **93**, 1540–1544 https://doi.org/10.1073/pnas.93.4.1540
83 Thalappilly, S., Suliman, M., Gayet, O., Soubeyran, P., Hermant, A., Lecine, P. et al. (2008) Identification of multi-SH3 domain-containing protein interactome in pancreatic cancer: a yeast two-hybrid approach. *PROTEOMICS* **8**, 3071–3081 https://doi.org/10.1002/pmic.200701157
84 Lu, J. and Gao, F.-H. (2016) Role and molecular mechanism of heterogeneous nuclear ribonucleoprotein K in tumor development and progression (Review). *Biomed. Rep.* **4**, 657–663 https://doi.org/10.3892/br.2016.642
85 Gerlach, H., Laumann, V., Martens, S., Becker, C.F.W., Goody, R.S. and Geyer, M. (2010) HIV-1 Nef membrane association depends on charge, curvature, composition and sequence. *Nat. Chem. Biol.* **6**, 46–53 https://doi.org/10.1038/nchembio.268
86 Collette, Y., Dutartre, H., Benziane, A., Ramos-Morales, F., Benarous, R., Harris, M. et al. (1996) Physical and functional interaction of Nef with Lck HIV-1 Nef-INDUCED T-CELL SIGNALING DEFECTS. *J. Biol. Chem.* **271**, 6333–6341 https://doi.org/10.1074/jbc.271.11.6333
87 Greenway, A.L., Dutartre, H., Allen, K., McPhee, D.A., Olive, D. and Collette, Y. (1999) Simian immunodeficiency virus and human immunodeficiency virus type 1 Nef proteins show distinct patterns and mechanisms of Src kinase activation. *J. Virol.* **73**, 6152–6158 https://doi.org/10.1128/JVI.73.7.6152-6158.1999
88 Betzi, S., Restouin, A., Opi, S., Arold, S.T., Parrot, I., Guerlesquin, F. et al. (2007) Protein–protein interaction inhibition (2P2I) combining high throughput and virtual screening: application to the HIV-1 Nef protein. *Proc. Natl Acad. Sci. U.S.A.* **104**, 19256–19261 https://doi.org/10.1073/pnas.0707130104

Supplementary materials

Supplementary Figures

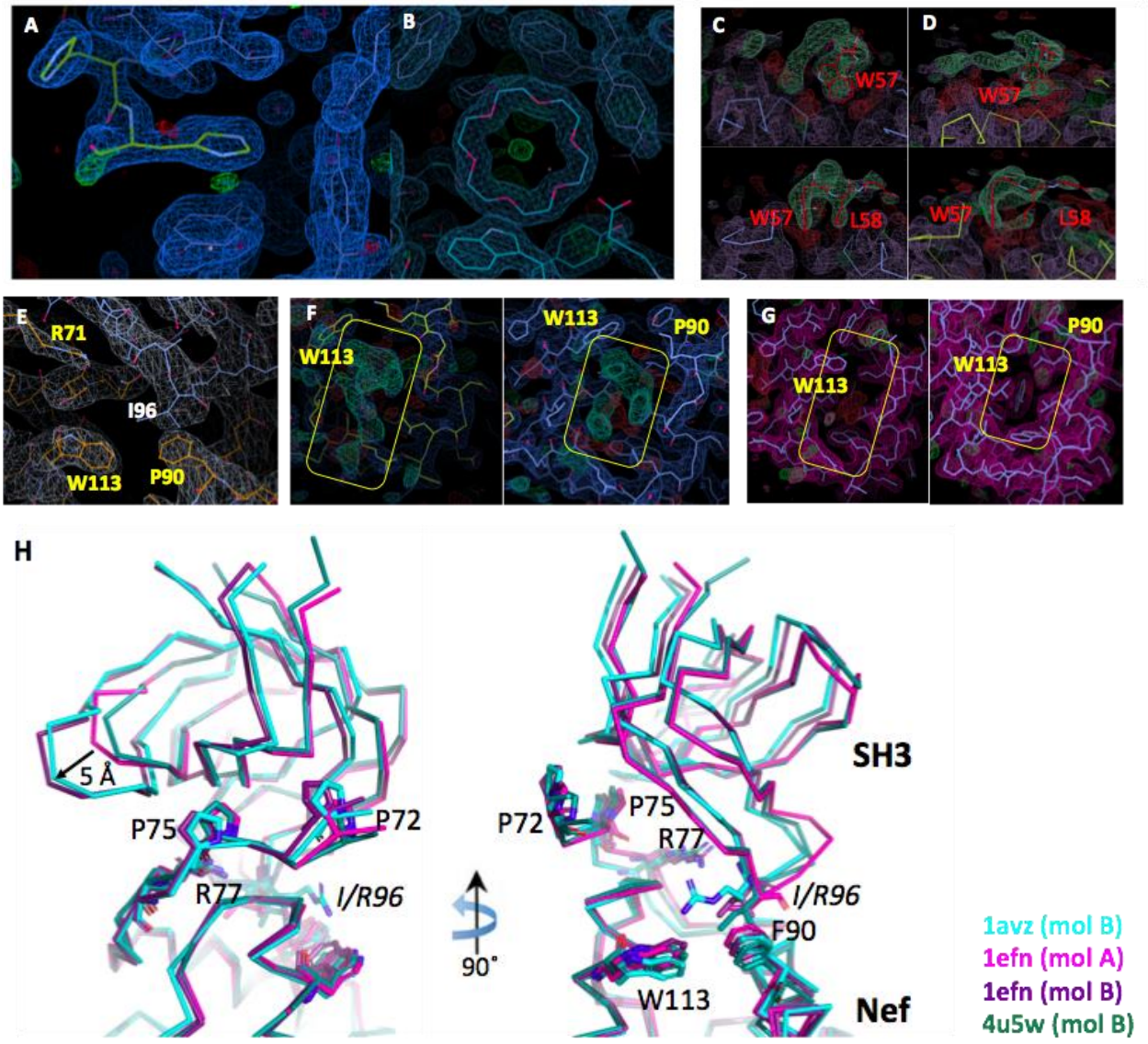

Fig. S1. A,B) Crystallization enhancement of Fyn SH3 domains. **A)** The second histidine of the Fyn_{R96I} mutant's C-terminal hexa-histidine tag forms pi-stacking interactions with a tyrosine from a symmetry related molecule. Contour level 1.5 RMSD. **B)** View onto the circular 18-crown-6 molecule found intercalated between two Fyn_{R96W} SH3 domains in the crystal lattice. **C)** Residual unattributed electron density observed in the α1-α2 groove of Nef–Fyn_{R96I} (PDB ID 1EFN). Top and bottom are 90° views of chain B. A fitted $W_{57}L$ sequence is shown in red. **D)** Top and bottom are 90° views of chain D. Phases were obtained from (PDB ID 1EFN). Contour level of the 2FoFc was 0.8 RMSD (green). **E)** View into the SF2 Nef–Fyn_{R96I} interface. For consistency, LAI numbering has been used for SF2 Nef (carbons in orange). **F)** Residual nonattributed electron density observed in the hydrophobic crevice of Nef–Fyn_{R96I} (1EFN). Contour level: 2FoFc:0.8 RMSD, FoFc: ±2.7 RMSD (green and red); *Left panel:* chain B; *Right panel*: chain D. **G)** The hydrophobic crevice of Nef–Fyn_{R96W} (4D8D) is devoid of such density. *Left panel:* chain B; *Right panel*: chain D. Same contour level as in (F). **H)** Malleability of the Nef–SH3 binding surface. 90° views of colour-coded superimposition of Nef core domains (bottom) bound to SH3 domains

(top). Complexes were aligned with respect to Nef, illustrating the positional variations for the SH3 domains. Key residues highlighted as sticks are those from the $P_{72}xxP_{75}xR_{72}$ motif, the gatekeepers F90 and W113, and the SH3 position 96 (either arginine or isoleucine, shown in italics). PDB entries are given in the same colour as the structures, with the chain name of the Nef molecule given in parentheses. 1avz: Nef_{LAI}–Fyn_{R96}, 1efn: $Nef_{LAI,\ T71R}$–Fyn_{R96I}, 4u5w: Nef_{SF2}–Hck SH2-SH3 (SH2 not shown). The arrow shows the difference between the C^{α}s of the SH3 position 127 (Fyn numbering).

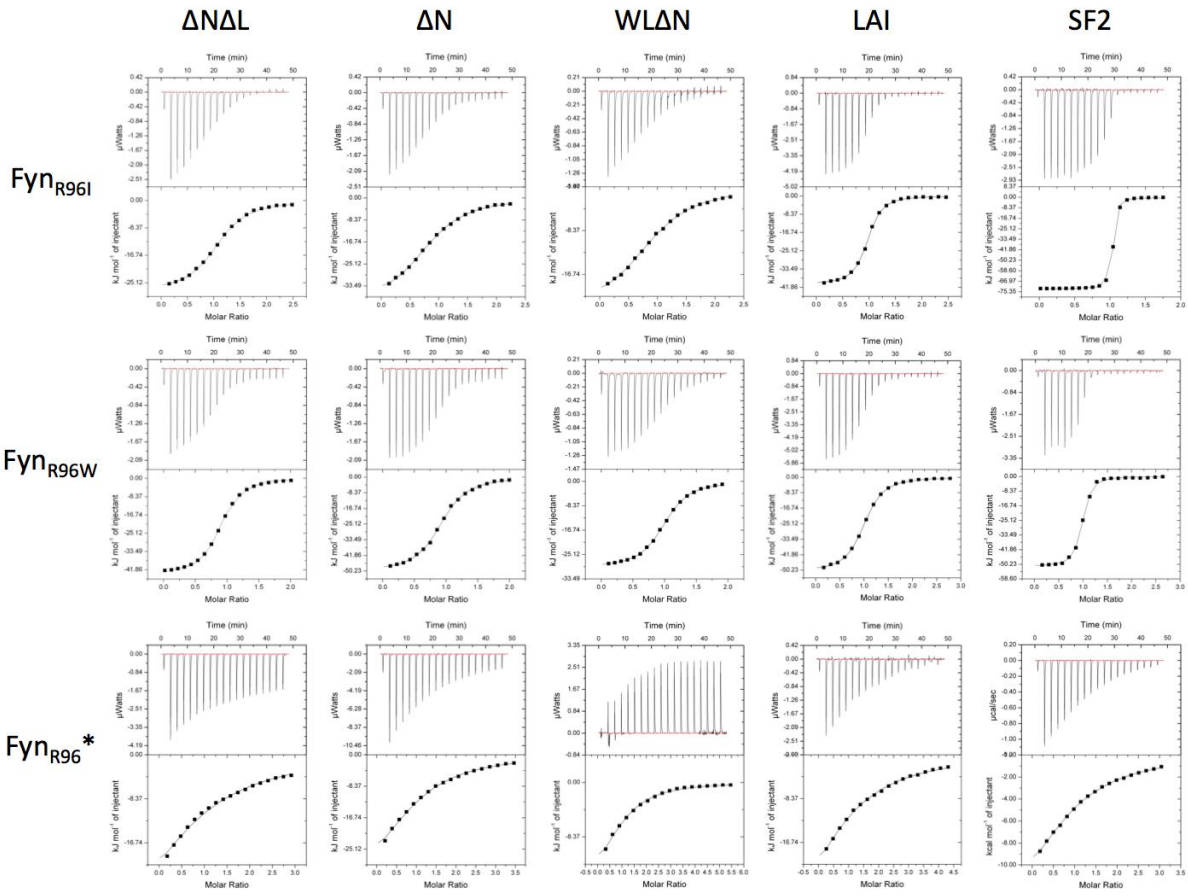

Fig. S2. Influence of flexible regions on the thermodynamics of SH3 binding by Nef. ITC curves were established at 25°C by titrating Fyn SH3 domains from the syringe onto Nef in the measurement cell (see Methods). (*) The C-value of the titration was too low to establish N, so it was fixed at 1 based on the known Nef–SH3 stoichiometry.

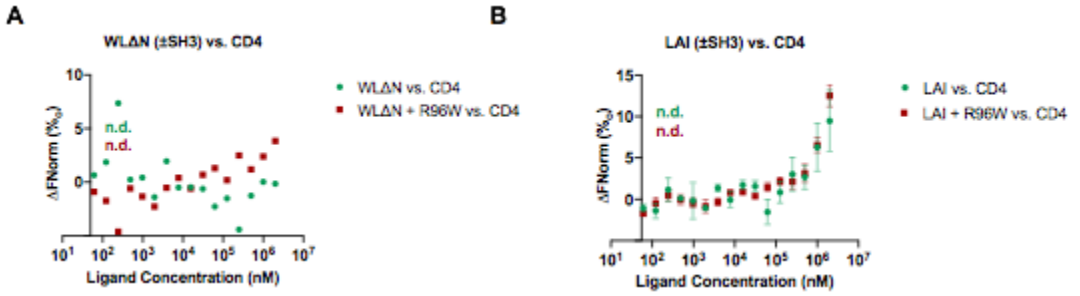

Fig. S3. The presence of an SH3 domain does not enhance Nef's interaction with a CD4 peptide. MST data were collected at 22 ˚C. Nef was labeled and used at a fixed concentration of 10–50 nM. The SH3 domain was added at a final concentration of 50 µM to form the Nef–SH3 complex before adding the unlabeled peptide. **A)** WLΔN vs. CD4 (green) or CD4+R96W (brown).**B)** LAI vs. CD4 (green) or CD4+R96W (brown)

Fig. S4. (continued on next page)

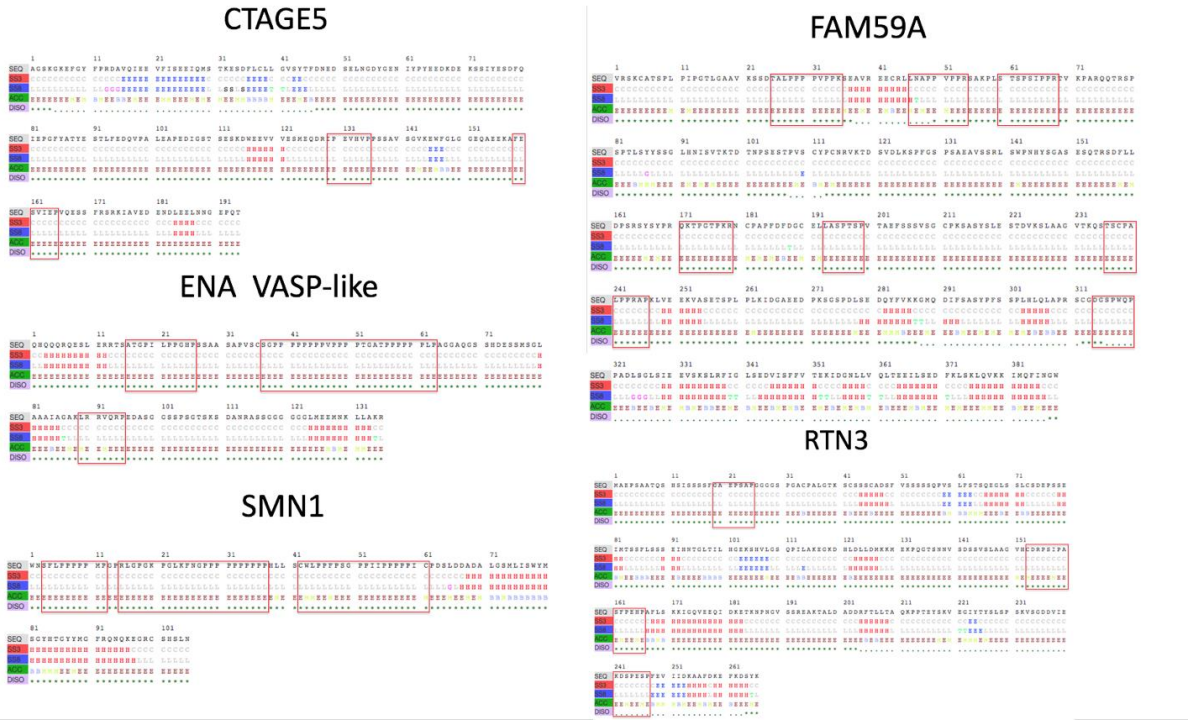

Fig. S4. RaptorX DSSP assigns three or eight secondary structure states which are assigned as follows: 3_{10}-helix turn (G), α-helix (H), π-helix (I), β-turn (T), β-strand (E), β-bridge (B), high-curvature loop (S), and irregular (L-for eight state or C-for three state). Solvent accessibility is assigned by: buried (B), medium exposed (M), and exposed (E). Disorder prediction is annotated by an asterisk (*) indicating ordered and a period (.) indicating disordered. Putative SH3-binding PR motifs were identified using ELM.

Supplementary Tables

Table S1. Crystallographic data collection and structure refinement statistics of unliganded Fyn_{R96I} and Fyn_{R96W} SH3 domain

	Fyn_{R96W}	Fyn_{R96I} (form I)	Fyn_{R96I} (form II)	Fyn_{R96I}(form I)	Fyn_{R96W}
Data Collection					
Space group	$P4_12_12$	$P4_1$	$P42_12$	$P4_1$	$P4_12_12$
Cell dimensions a, b, c (Å)	52.1, 52.1, 53.3	41.9, 41.9, 32.8	90.4, 90.4, 26.8	41.5, 41.5, 32.6	51.5, 51.5, 51.9
Resolution range (Å) [a]	30.0–2.60 (2.70–2.60)	20.9–1.76 (1.80–1.76)	23.0–2.20 (2.32–2.20)	29.36–1.343 (1.391–1.343)	36.54–1.576 (1.633–1.576)
Completeness (%)	91.9 (58.2)	98.5 (92.7)	99.9 (99.9)	98.58 (87.67)	99.83 (98.38)
Total number of reflections	12,939	14,820	29,780	155919 (8237)	258718 (24606)
Number of unique reflections	2,270	5,700	5,956	12432 (1125)	10112 (988)
Multiplicity	5.7 (2.7)	2.6 (2.3)	5.0 (4.7)	12.5 (7.3)	25.6 (24.9)
R_{merge} [b]	0.15 (0.63)	0.05 (0.08)	12.2 (0.52)	0.07325 (1.3744)	0.06273 (2.2542)
I/σI	13.4 (1.7)	25.2 (12.3)	14.3 (3.8)	20.23 (0.76)	29.66 (0.91)
Number of molecules in ASU	1	1	2	1	1
Solvent content (%)	44.85	31.34	27.74	31.0	23.0
Refinement					
Resolution range (Å)	30–2.6 (2.7–2.6)	20.9–1.8 (1.8–1.76)	23.0–2.2 (2.26–2.2)	29.36–1.343 (1.391–1.343)	36.54–1.576 (1.633–1.576)
Number of reflections used	2119	5235	5734	12376 (1095)	10095 (972)
R_{cryst} (%) [c]	20.2 (26.4)	16.6 (21.1)	18.4 (32.1)	18.1 (34.95)	19.02 (31.16)
R_{free} (%) [d]	28.2 (46.1)	22.2 (25.6)	24.3 (37.6)	20.2 (41.34)	20.87 (30.96)
Number of non-H atoms	502	507	1029	584	571
R.M.S. deviations					
Bond lengths (Å)	0.017	0.022	0.021	0.005	0.011
Bond angles (°)	1.70	1.94	1.78	0.99	1.38
PDB accession number	3H0F	3H0H	3H0I	6IPY	6IPZ

[a] Values in parentheses are for the highest-resolution shell.

[b] $R_{merge} = \Sigma_{hkl}\Sigma_i |I_i(hkl) - \langle I(hkl)\rangle| / \Sigma_{hkl} \Sigma_i I_i(hkl)$, where $I_i(hkl)$ and $\langle I(hkl)\rangle$ are the observed individual and mean intensities of a reflection with indices *hkl*; and $\sum hkl$ is the sum over all reflections.

[c] $R_{cryst} = \Sigma_h ||Fo_h| - |Fc_h|| / \Sigma_h |Fo_h|$

[d] All measured reflections were included in refinement, except the 5–10% that were used to calculate R_{free}. In the Nef complexes, arginine 77 from the Nef PxxPxR77 motif binds to Fyn D100 which is situated in the center of the RT-loop (See, 1EFN, 1AVZ, 4D8D and 7D7S). A crystallographic mimicry of this intramolecular salt bridge was incorporated in Fyn_{R96I} Form I crystals, and in one of the two molecules of the asymmetric unit of Fyn_{R96} Form II. Therefore, we took only the remaining native-like molecule Fyn_{R96} Form II as a 'free-state' structure.

Table S2. Crystallographic data analysis and structure refinement statistics of the LΔN–Fyn$_{R96W}$ SH3 complex

	LΔN–Fyn$_{R96W}$	SF2 Nef–Fyn$_{R96I}$
Data Collection		
Space group	$P6_522$	$P6_422$
Cell dimensions a, b, c (Å)	108.01, 108.01, 224.96	122.11, 122.11, 145.89
Resolution range (Å) [a]	52.5–2.52 (2.52–2.67)	48.6–3.32/3.71[e] (3.46–3.32)
Completeness (%)	99.2 (93.6)	92.4 (42.1)[e]
Total number of reflections	198,135	1,431,398
Number of unique reflections	26775	9209
Multiplicity	7.4 (6.3)	155.4 (165.4)
R_{merge} [b]	0.067 (0.319)	0.218 (9.136) [0.018 (0.710)][f]
I/σI	17.8 (2.3)	33.6 (1.1)
Number of molecules in ASU	2 Nef, 2 SH3	2 Nef, 2 SH3
Solvent content (%)	55.1	46.4
Refinement		
Resolution range (Å)	52.51 - 2.52	48.6–3.32/3.71[e] (3.41–3.32)
Number of reflections used (Free)	26775 (1348)	9205 (365)
R_{cryst} (%) [c]	21.2	27.8
R_{free} (%) [d]	23.9	30.7
Number of non-H atoms	2775	2737
R.M.S. deviations		
Bond lengths (Å)	0.008	0.009
Bond angles (°)	0.994	1.240
PDB accession number	4D8D	7D7S

[a] Values in parentheses are for the highest-resolution shell.

[b] $R_{merge} = \Sigma_{hkl}\Sigma_i |I_i(hkl) - \langle I(hkl)\rangle|/\Sigma_{hkl}\Sigma_i I_i(hkl)$, where Ii(hkl) and <I(hkl)> are the observed individual and mean intensities of a reflection with indices hkl; and ∑hkl is the sum over all reflections.

[c] $R_{cryst} = \Sigma_h||Fo_h| - |Fc_h|| / \Sigma_h|Fo_h|$

[d] All measured reflections were included in the refinement, except the 5–10% that were used to calculate R_{free}.

[e] data was cut anisotropically, using Staraniso.
Worst diffraction limit: 3.74 Å at reflection 0 0 39 in direction c*
Best diffraction: 3.324 Å at reflection 24 3 26 in direction 0.676 a* + 0.084 b* + 0.732 c*

[f] Rp.i.m is given in square brackets because it reflects the data precision better at the low resolution and high data redundancy of this data set.

Table S3. Occupancy survey of Nef α1-α2 by H1/$W_{57}L$

PDB ID	H1	E_{160}xxxLL motif	$W_{57}L$	α1-α2 grove	Nef Isolate	Method and resolution	Composition
2NEF	Deleted	Deleted	Bound to α1-α2 grove	Occupied by $W_{57}L$	LW123	NMR	NefΔ2-55Δ159-173
4NEE	Deleted	Resolved	Unknown	Unoccupied	HXB2	X-ray 2.88 Å	NefΔ2-53Δ204-206 bound to AP-2 alpha/sigma2 complex
3RBB	Deleted	Resolved	Not resolved	Occupied by E_{160}xxxLL	SF2	X-ray 2.35 Å	NefΔ2-44 bound to HCK SH3
6CRI	Resolved	Resolved	Not resolved	Occupied by H1	NL4–3	EM 6.80 Å	Nef full length bound to AP-1/Arf1/tetherin
6CM9	Resolved	Not resolved	Not resolved	Occupied by H1	NL4–3	EM 3.73 Å	Nef full length bound to AP-1/Arf1/tetherin
1AVZ	Deleted	Not resolved	Deleted	Unoccupied	LAI	X-ray 3.00 Å	NefΔ2-57 bound to Fyn SH3
4U5W	Deleted	Not resolved	Deleted	Occupied by dimer Nef	SF2	X-ray 1.86 Å	NefΔ2-61Δ210 bound to HCK SH3-SH2
4EN2	Resolved	Not resolved	Not resolved	Occupied by H1	NL4–3	X-ray 2.58 Å	Nef full length bound to MHC-1 cytoplasmic domain/Mu1 adaptin of AP-1
6B72	Deleted	Not resolved	Resolved	Occupied by $W_{57}L$ from adjacent Nef	SF2	X-ray 3.20 Å	NefΔ2-56Δ208-210 bound to octyl-glucoside molecule

Table S4. Clones obtained from yeast two-hybrid screening using an Hck SH3 domain as bait

Hck-SH3 Interactors	Gene ID	Hck-SH3 Interactors	Gene ID
abl-interactor 1	10006	ATN1	1822
Alix / PDCD6IP	10015	PDE4DIP	9659
CTAGE5	4253	SMN1	6606
Ena/VASP-like	51466	PIK3C2B	5287
FAM59A	64762	COL4A2	1284
GFAP	2670	LTBP4	8425
HNRPK	3190	BAT2	7916
RTN3	10313	FAM59B	150946
SRRT / ARS2	51593	LZTS2	84445
KHDRBS1	10657	BCAR1	9564
SF3B4	10262	SERINC1	57515
SOS2	6655	EFS	10278
SYNGAP1	8831	C9orf169	375791
DAB2IP	153090		

Table S5. Clones obtained from yeast two-hybrid screening using a Fyn_{R96I} SH3 domain as bait

Fyn_{R96I}-SH3 Interactors	Gene ID	Fyn_{R96I}-SH3 Interactors	Gene ID
Alix / PDCD6IP	10015	RhoGAP	-
CTAGE5	4253	SMC4L1	10051
SMN1	6606	HNRPK	3190
Ferritin	-	MCRS1	10445
IRF3	3661	ECSIT	51295
FAM59A	64762	PP2A	-
KHDRBS1	10657	YLPM1	56252
Syntaxin binding	-	YY1	7528

Supplementary Data

SD1.1 MD Simulations

Hydrogen bond analysis of Nef-A and Nef-C.

Molecular dynamics simulations were carried out in triplicate for apo Nef (Nef-A) and Nef complexed to Fyn_{R96I} (Nef-C), using as a template the 2.5 Å resolution crystal structure of LAI Nef_{T71R} WLΔN structure to Fyn_{R96I} (PDB ID 1EFN). The intramolecular H-bond calculation showed Nef-A forming 102 ± 4 H-bonds, while Nef-C formed 99 ± 4 H-bonds over the course of the simulation, showing that Nef in both settings was similarly stable, with a difference of 2 H-bonds **(Fig. S5 A)**. A lesser number of H-intramolecular H-bonds in Nef-C were the result of H-bonds implicated in the interaction with SH3 domain. Intermolecular H-bond analysis for Nef-C showed an increasing number of H-bonds formed between Nef and the SH3 domain over the course of time (**Fig. S5 B)**. The number of H-bonds between Nef and the SH3 domain in the starting structure were found to be 6 ± 1, while the average number of H-bonds formed between Nef and the SH3 domain over time was 13 ± 2, which explains the slight increase in stability for Nef-C after the first 45–50 nanoseconds, a phenomenon which is also observed in RMSD calculations **(Fig. 3A)**.

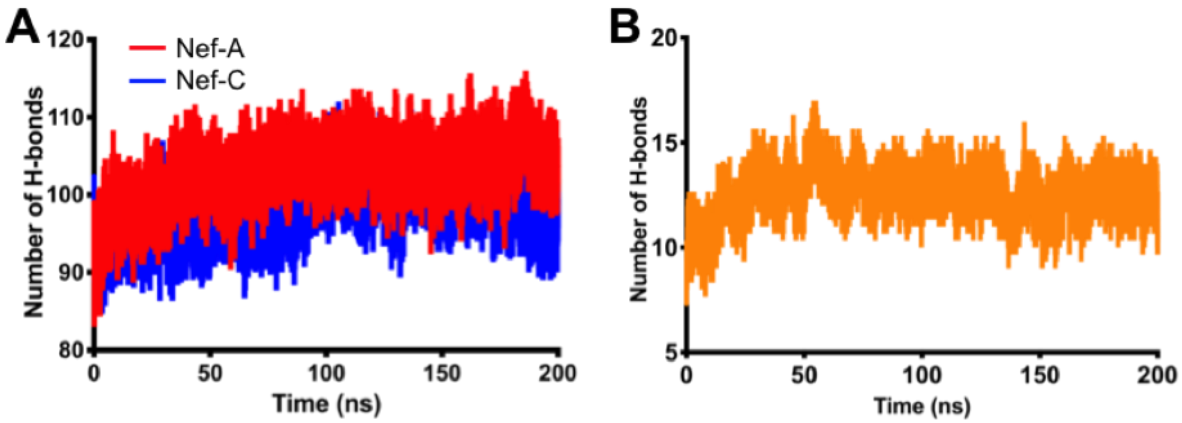

Figure S5. A) The average number of intramolecular H-bonds formed for Nef against time in Nef-A and Nef-C. **B)** The average number of intermolecular H-bonds formed between Nef and the SH3 domain against time in Nef-C.

S1.1.1 Dynamics of the α1–α2 groove

SH3 binding to Nef (in particular Fyn_{R96I}) enhanced the association of H1 with the α1–α2 groove. The α1–α2 groove was very stable in both cases, with maximal RMSD values on the Cα atoms remaining within 1.0 Å from the initial structure. The average RMSD of the α1–α2 groove from the initial structure of Nef-A was found to be 1.06 ± 0.13 Å, whereas for Nef-C it was 1.01 ± 0.12 Å **(Fig. S6 A)**. To further confirm the stability, we calculated the average RMSD for the α1–α2 groove using the average structure from the simulation. The RMSD calculation showed Nef-A to be of 1.13 ± 0.21 Å, while Nef-C showed an RMSD of 1.09 ± 0.19 Å **(Fig. S6 B)**. We also calculated the average RMSD for the α1–α2 groove between frames for 50 ns to 200 ns, excluding the initial part of the simulation, in which Nef-C fluctuates before stabilizing. The average RMSD for the α1–α2 groove in Nef-A was found to be 1.08 ± 0.10 Å, while that in Nef-C was 0.96 ± 0.08 Å **(Fig. S6 C)**. We also performed an average RMSF calculation for the α1–α2 groove, and found that the RMSF of the α1–α2 groove residues in Nef-A was 0.74 ± 0.30 Å, while the RMSF in Nef-C was found to be 0.65 ± 0.27 Å **(Fig. S6 D)**. We also calculated the RMSF for the α1–α2 groove between 50 ns to 200 ns and found the average RMSF of the α1–α2 groove in Nef-A to be 0.49 ± 0.12 Å, while the RMSF for Nef-C was 0.44 ± 0.10 Å **(S6 E Fig)**. These data suggest that the α1–α2 groove region is slightly more stable in the structure of Nef-C than in Nef-A.

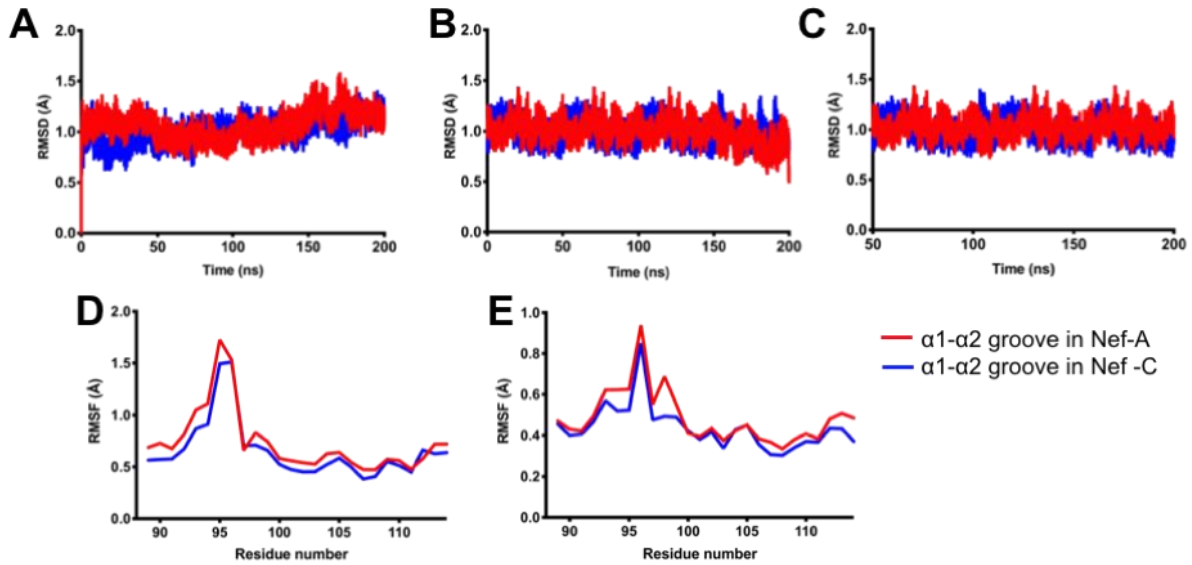

Figure S6. A) Average Cα RMSD values over simulation time for the α1–α2 groove in Nef-A and Nef-C, using the initial structure as a reference ; **B)** as (A), but using the overall average structure as reference, and **C)** using the 50 ns to 200 ns average as reference structure. **D)** Average CαRMSF values vs. residue numbers for the α1–α2 groove in Nef-A and Nef-C and **E)** between 50 ns and 200 ns.

SD1.1.2 Dynamics of residues 77–81

Residues 77–81 were very stable in both cases, with maximal RMSD values on the Cα atoms not exceeding 1.0 Å from the initial structure. The average RMSD of residues 77–81 from the initial structure of Nef-A was found to be 0.38 ± 0.09 Å, whereas for Nef-C it was 0.34 ± 0.07 Å **(Fig. S7 A)**. To further confirm the stability, we calculated the average RMSD for residues 77–81 using the average structure from the simulation. The RMSD calculation showed Nef-A to be of 0.46 ± 0.10 Å, while Nef-C showed an RMSD of 0.36 ± 0.07 Å **(Fig. S7 B)**. We also calculated the average RMSD for residues 77–81 between frames for 50 ns to 200 ns, excluding the initial part of the simulation in which the Nef-C fluctuates before stabilizing. The average RMSD for residues 77–81 in Nef-A was found to be 0.45 ± 0.09 Å, while in Nef-C it was 0.35 ± 0.07 Å **(Fig. S7 C)**. We also performed the average RMSF calculation for residues 77–81, and found that the RMSF of residues 77–81 in Nef-A was 0.35 ± 0.05 Å, while the RMSF in Nef-C was found to be 0.27 ± 0.02 Å **(Fig. S7 D)**. We also calculated the RMSF for residues 77–81 between 50 ns and 200 ns, and found the average RMSF of residues 77–81 in Nef-A to be 0.33 ± 0.04 Å, while the RMSF for Nef-C was 0.25 ± 0.02 Å **(Fig. S7 E)**. These data suggest that residues 77–81 are more stable in the structure of Nef-C than in Nef-A.

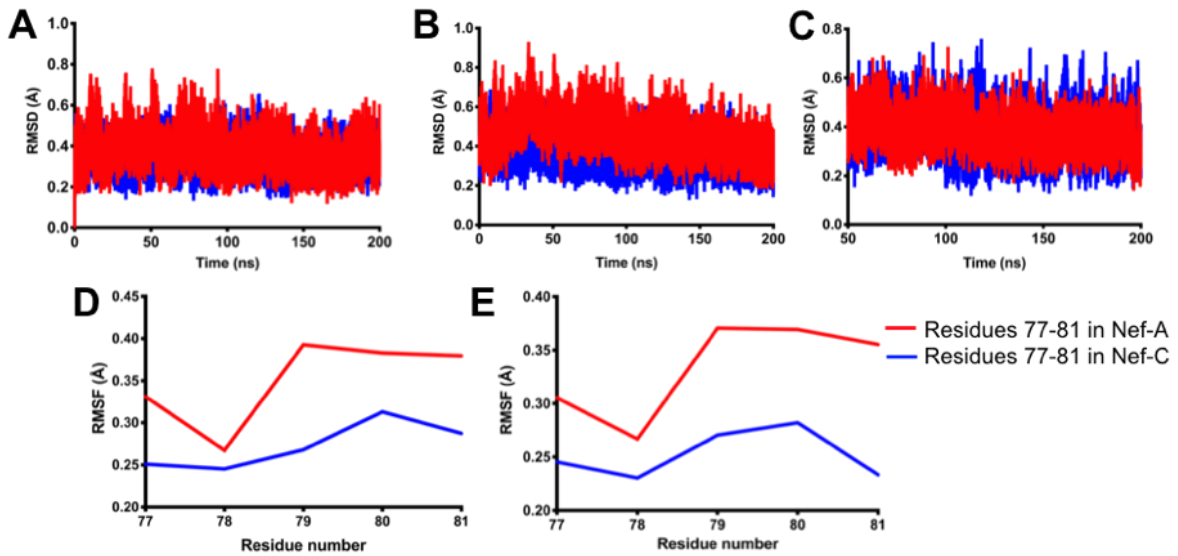

Figure S7. A) Average CαRMSD values using initial structure as a function of time for residues 77–81 in Nef-A and Nef-C; **B)** using average structure, and **C)** between 50 ns and 200 ns using average structure. **D)** Average CαRMSF values vs residue numbers for residues 77–81 in Nef-A and Nef-C, and **E)** between 50 ns and 200 ns.

SD1.1.3 Dynamics of residues 121–139

The residues 121–139 in both cases showed maximal RMSD values with the Cα atoms not exceeding 1.0 Å from the initial structure. The average RMSD of residues 121–139 from the initial structure of Nef-A was found to be 0.91 ± 0.09 Å, whereas that for Nef-C was 0.87 ± 0.08 Å **(Fig. S8 A)**. To further confirm the stability, we calculated the average RMSD for residues 121–139 using the average structure from the simulation. The RMSD calculation showed Nef-A to be 0.87 ± 0.10 Å, while Nef-C showed an RMSD of 0.76 ± 0.17 Å **(Fig. S8 B)**. We also calculated the average RMSD for residues 121–139 between frames for 50 ns to 200 ns, excluding the initial part of the simulation in which the Nef-C fluctuates before stabilizing. The average RMSD for residues 121–139 in Nef-A was found to be 0.86 ± 0.10 Å, while in Nef-C it was 0.71 ± 0.09 Å **(Fig. S8 C)**. We calculated the average RMSF for residues 121–139, and found that the RMSF of residues 121–139 in Nef-A was 0.54 ± 0.20 Å, while the RMSF in Nef-C was found to be 0.48 ± 0.15 Å **(Fig. S8 D)**. We also calculated the RMSF for the residues 121–139 between 50 ns and 200 ns, and found the average RMSF of residues 121–139 in Nef-A to be 0.50 ± 0.15 Å, while the RMSF for Nef-C was 0.44 ± 0.13 Å **(Fig. S8 E)**. These data suggest that residues 121–139 are consistently more stable in the structure of Nef-C than in Nef-A.

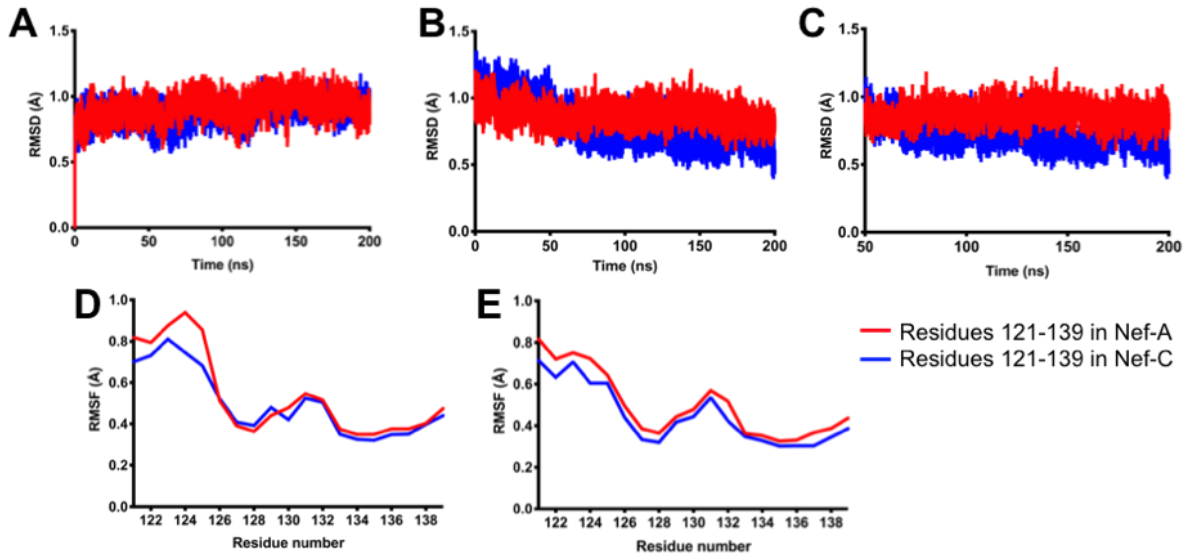

Figure S8. A) Average CαRMSD values using the initial structure as a function of time for residues 121–139 in Nef-A and Nef-C; **B)** using average structure and **C)** between 50 ns and 200 ns using average structure. **D)** Average CαRMSF values vs. residue numbers for residues 121–139 in Nef-A and Nef-C, and **E)** between 50 ns and 200 ns.

SD1.2 Analysis of the flexibility of the Nef–SH3 interface

To observe the influence of position 96 on the overall binding between Nef and SH3 domains, we superimposed all Nef–SH3 domains, including the structures of HIV-1 Nef bound to engineered high-affinity Hck SH3 domains with mutations in the RT loop. The superimposition of all SH3-bound structures shows marked flexibility in the positioning of the SH3 domain relative to the tertiary binding site (**Fig. 5**). This plasticity is already apparent between the two Nef–SH3 complexes contained in the asymmetric unit of the crystal structure obtained in the space group P6522 (Nef–FynR96I and Nef–Fyn_{R96} [note that the P6522 crystal structure of Nef–Fyn_{R96} only contained one complex and one apo Nef] (22)). In this crystal lattice, the SH3 domain of one complex is implicated in weak crystal contacts (complex B), which may distort the Nef–SH3 interface, whereas the SH3 domain of the other complex (complex A) is only connected to its cognate Nef molecule. Within complexes A and B, all Nef–Fyn variants (R96, R96I and R96W) superimpose closely, showing that it is the crystal lattice, apart from the different amino acids in SH3 position 96, that caused the change in relative orientation. Nef–Hck SH2-SH3 crystallized in a different space group (P1). Both complexes found in the asymmetric unit superimpose closely and are overall more similar to the Nef–Fyn SH3 complexes A, supporting the contention that complexes B are affected by crystal contacts. Nef has also been crystallized bound to an engineered high-affinity Hck SH3, in which the wild-type RT-loop sequence EAI*HHE was replaced by YSPF*SW (*marks the position corresponding to Fyn position 96) (71). The two complexes found in the asymmetric unit (space group P212121) superimpose closely but are markedly different from all other Nef–SH3 complexes, including the Nef–Hck SH2-SH3 complex.